Journal Pre-proofs

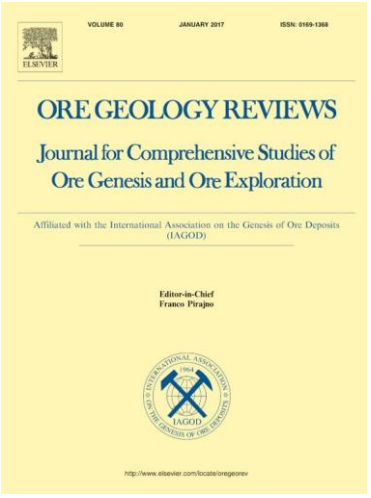

The world-class Koushk Zn-Pb deposit, Central Iran: A genetic model for vent-proximal shale-hosted massive sulfide (SHMS) deposits – Based on paragenesis and stable isotope geochemistry

Abdorrahman Rajabi, Pura Alfonso, Carles Canet, Ebrahim Rastad, Shojaedin Niroomand, Soroush Modabberi, Pouria Mahmoodi

PII: S0169-1368(19)30835-2
DOI: https://doi.org/10.1016/j.oregeorev.2020.103654
Reference: OREGEO 103654

To appear in: *Ore Geology Reviews*

Received Date: 18 September 2019
Revised Date: 5 June 2020
Accepted Date: 12 June 2020

Please cite this article as: A. Rajabi, P. Alfonso, C. Canet, E. Rastad, S. Niroomand, S. Modabberi, P. Mahmoodi, The world-class Koushk Zn-Pb deposit, Central Iran: A genetic model for vent-proximal shale-hosted massive sulfide (SHMS) deposits – Based on paragenesis and stable isotope geochemistry, *Ore Geology Reviews* (2020), doi: https://doi.org/10.1016/j.oregeorev.2020.103654

The world-class Koushk Zn-Pb deposit, Central Iran: a genetic model for vent-proximal shale-hosted massive sulfide (SHMS) deposits – based on paragenesis and stable isotope geochemistry

Abdorrahman Rajabi[a]*, Pura Alfonso[b], Carles Canet[c], Ebrahim Rastad[d], Shojaedin Niroomand[a], Soroush Modabberi[a], Pouria Mahmoodi[d]

a- School of Geology, College of Science, University of Tehran, Tehran, Iran

b- Dept. d'Enginyeria Minera, Industrial i TIC, Universitat Politècnica de Catalunya, Av. de les Bases de Manresa 61-73 o8242 Manresa, Spain

c- Centro de Ciencias de la Atmósfera, Universidad Nacional Autónoma de México, Del. Coyoacán, 04150 Ciudad de México, Mexico

d- Department of Geology, Faculty of Basic Sciences, Tarbiat Modares University, Tehran 14115-175, Iran

⁎ **Corresponding author:** rahman.rajabi@ut.ac.ir (A. Rajabi).

Abstract

The Koushk Zn-Pb deposit is the largest known and least deformed and non-metamorphosed Early Cambrian shale-hosted massive sulfide (SHMS) deposit at Central Iran. The current remaining reserves are estimated to be greater than 14 Mt ore, averaging 7% Zn and 1.5% Pb; the primary resources ore of the deposit is estimated to be more than 60 Mt.

At this deposit, different hydrothermal ore styles (bedded ore, vent complex, and feeder zone) are well preserved within the Lower Cambrian black siltstones and shales. According to fluid- rock interaction and different ore-forming processes in SHMS systems, these ore facies with extensive hydrothermal alteration provide unique conditions to understand critical textural and geochemical frameworks to present a genetic model. In this research, we focus on different paragenetic stages of sulfide mineralization and fluid-rock interactions in different ore styles from the Koushk SHMS deposits. The paragenetic relationship provides the context for the interpretation of stable isotopes (S, C, and O) in hydrothermal sulfides and carbonates.

Detailed petrography and paragenetic studies represent three major generations of sulfide mineralizations at different ore zones: (1) stage I includes very fine-grained (<6 μm) framboids, spherulite pyrite (py_1), associated with minor fine-grained disseminated sphalerite (sp_1), and galena (sp_2); (2) Stage II is composed of a diagenetic intergrowth of coarse-grained framboids and spherulite pyrite, packed polyspherulite aggregates and pyrite nodules (py_2) replacing diagenetic barite and carbonate nodules, and are followed with coarse-grained sphalerite (sp_2) and galena (gn_2) that replace former sulfides and barite, deposited as disseminated, laminated and sulfide-rich banded textures; (3) stage III of sulfide mineralization is characterized by a vent complex development (VCD) over the feeder zone, hydrothermal brecciation, dissolution of rock-forming minerals, and extensive replacement of earlier sulfides and barite, leading to deposition of stage III of ore sulfides. The oxygen and carbon isotopes values, for fluid in equilibrium with hydrothermal calcite and dolomite in this deposit range from $\delta^{18}O$ +8 to +16.7 ‰ and $\delta^{13}C$ from -8.3 to -4.3 ‰, are generally compatible with basinal brines and formation water as fluid sources. In addition, highly positive $\delta^{34}S$ values of hydrothermal sulfides (+6.5 to +36.7 ‰) in different ore stages of the Koushk deposit are consonant with other SHMS deposits.

Textural relationships and S isotope data reveal that the contribution of bacterial sulfate reduction (BSR) in the Zn-Pb mineralization is not so significant, but the thermochemical sulfate reduction (TSR) nd direct barite replacement could provide sufficient sulfur for the main sulfide mineralization in the SHMS deposits. Also, the data presented in this paper are against a syngenetic, purely synsedimentary-exhalative model, and give prominence to that vent-proximal SHMS deposits formed predominantly during the diagenesis in the uppermost sediment pile and replacement of host rocks during vent complex development (VCD) processes.

Keywords: Koushk, SHMS Zn-Pb, SEDEX, stable isotopes, thermochemical sulfate reduction (TSR), vent complex development (VCD)

Introduction

Shale-hosted massive sulfide (SHMS) ore deposits, that previously described as sedimentary exhalative (SEDEX; Carne and Cathro, 1982; Goodfellow et al., 1993), are significant sources of zinc and lead, and usually form laterally extensive stratiform to stratabound accumulations of sulfides hosted in black shales and siltstones. SHMS mineralization is considered to form by deposition of sulfides at the seafloor from hydrothermal fluids that are thought to exhale from a vent complex. Preservation of feeder and vent complex is rare at most of these deposits, so-called vent-distal SHMS, and only very few deposits, known as vent-proximal SHMS deposits, show a clear relationship between the feeder pipe and the overlying sulfide mineralization (e.g., Sangster, 2002; 2018; Rajabi et al., 2015a,b; Magnall et al., 2016a). The Zarigan–Chahmir basin (ZCB, Fig. 1), located in Posht-e-Badam block of the Central Iranian Microcontinent

(CIM), hosts several SHMS deposits, including the Koushk, Chahmir, and Zarigan deposits, and Darreh-Dehu, Wedge, and Cheshmeh-Firouz occurrences (Fig. 1b), hosted in Early Cambrian volcano-sedimentary sequence (ECVSS). Koushk is the largest and economically most important SHMS Zn-Pb deposit in Iran. Although there are some ancient mining activities at the Koushk area, this deposit was first mined for zinc and lead in 1939. There is no accurate data on the primary resources of the deposit, but it is estimated to be more than 60 Mt, and its size (1500 m length, 65-150 m thickness) comparable to that of the Meggen (Germany), Anniv, and XY (Howards Pass, Canada) Zn-Pb deposits. Rajabi et al. (2012b) reported 20 Mt ore reserves for this deposit in 2012 and classified it as a vent-proximal SHMS mineralization. Its current remaining reserves are greater than 14 Mt ore, averaging 7% Zn and 1.5% Pb.

Most SHMS deposits worldwide have experienced extensive recrystallization and destruction of primary textures during post-ore deformation and metamorphism. Only a few deposits, such as McArthur River, Australia (Large et al., 1998), Macmillan Pass, Canada (Magnall et al., 2016a) and the Koushk and Chahmir deposits, central Iran, preserve most of their primary, synsedimentary features. Herein, we are going to focus on mineral phases from the vent complex and bedded ore, which are particularly well preserved in the Koushk deposit, in order to develop a better understanding of fluid rock interaction in the central up-flow zone of SHMS systems. We also present stable isotope (S, O, and C) data of specific mineral phases at the Koushk deposit, new data that can improve our understanding from the Cambrian SHMS mineralizations and ore-forming processes in vent-proximal SHMS deposits.

Geological and tectonic setting

The Zarigan-Chahmir basin (ZCB) is a significant back-arc rifting succession in the central lithotectonic domain of Posht-e-Badam block, also known as the Kashmar-Kerman structural

zone, in the CIM. The basin consists of non-metamorphosed, Early Cambrian marine sedimentary, and intercalated volcanic rocks (ECVSS; Rajabi et al., 2015a), covering the oldest Precambrian continental basement of Iran, and it is bordered by the Kuhbanan Fault to the east and the Posht-e-Badam Fault to the west (Fig. 1b).

In the ZCB, the oldest basement composed of the late Neoproterozoic metamorphic rocks of the Boneh-Shurow Complex (617−602 Ma). The Tashk Formation unconformably overlies this complex and consists of 2000 m-thick, well-stratified sequence of weakly metamorphosed to non-metamorphosed, sedimentary, and volcanic/volcaniclastic rocks (Fig. 2). The ECVSS sequence, which overlies the Tashk Formation, is about 1500−2000 m thick (Rajabi et al., 2015a) and consists of sandstones, volcaniclastic and tuffaceous rocks, intermediate to felsic and basaltic lavas, shales, black siltstones, dolomites and dolomitic limestones, and minor gypsum beds (Ramezani and Tucker, 2003; Rajabi et al., 2015a). U-Pb zircon dating gave 528.2 ±0.8 Ma age for the dacitic porphyries and rhyodacites of the lower part of the ECVSS (Ramezani and Tucker, 2003). This sequence is unconformably overlain by the Lowe Cambrian red sandstones and conglomerates (Lalun/Dahu Fm.) and by the Middle Cambrian trilobite-bearing Mila Formation in the Zarigan and Chahmir areas (Föerster and Jafarzadeh, 1994; Rajabi et al., 2015a,b).

The evolution of the CIM is related to the assembly of Gondwana. One of the most significant geological features of the Posht-e-Badam block is an almost N-S magmatic belt, in the west and northwest of the ZCB (Fig. 1b), and the nature of igneous rocks of the ECVSS. This Early Cambrian magmatism was recently defined as a magmatic arc (Fig. 1b) developed along the Proto-Tethyan margin of the Gondwana supercontinent (Ramezani and Tucker, 2003; see Fig. 16 in Rajabi et al., 2015a). Rajabi et al. (2015a,b) reported geological and geochemical data that

support an extensional back-arc rifting in the eastern portion of the area. They suggested that the SHMS (e.g., Koushk and Chahmir) and iron oxide-apatite (IOA) deposits also formed in this geotectonic setting. The opening of the ZCB in the Posht-e-Badam block took place when the CIM broke up in the Late Neoproterozoic−Early Cambrian, due to the back-arc rifting of the continental margin, which happened coevally with the convergence of the Proto-Tethys along the continental margin (see figures 13 and 14 in Rajabi et al., 2015a).

Stratigraphy of the ECVSS and geology of the Koushk deposit

The geology of the basin and stratigraphy of the ECVSS have been described in detail by Rajabi et al. (2015a). The stratigraphic correlation scheme (Fig. 3) is applicable throughout the basin, based on sequence stratigraphic analysis of the ECVSS and geochemical data. The scheme is subdivided the system into two sub-sequences, defined from contemporaneous depositional and structural events recognizable across the basin (Fig. 3). Two main stages of a rift event for the ECVSS are proposed: (I) A syn-rift phase, related to the intra-basin extension, indicated by coarse-grained detrital sedimentary rocks and bimodal volcanism (lower part of the ECVSS). (II) A sag phase, comprising calcareous shales, siltstones, and carbonates (upper part of the ECVSS); sedimentation during this phase was controlled by basin subsidence and reactivation of the half-graben faults.

Two stratigraphic sequences have been identified in the Koushk mining district (Fig. 4): (*a*) an ore-bearing sequence that comprises the upper part of the ECVSS, and (*b*) a volcano-sedimentary sequence that includes tuffaceous rocks, shales, and limestones. Detailed stratigraphic studies indicated that the latter could be correlated with the lower part of the ECVSS in the ZCB (Rajabi et al., 2012b). In the southeastern part of the deposit, the ore-bearing sequence trends northwestwards, steeply dipping to the southwest; in the NW of the deposit, however, it changes

to a southwestward strike that gently dips to the SE (Fig. 4). The basal unit of this sequence consists of grey lithic crystal tuffs, rich in quartz, alkaline feldspars, and lithic fragments, overlain by locally dolomitized sandy to silty limestones, grading upwards to shales and siltstones. The calcareous siltstones and shales transition to fine-grained, organic matter-rich black siltstones and shales in the ore-bearing horizon, and are overlain by interbedded tuffs, shales and cherts. Limestones and massive cherty dolomites form the uppermost part of the ECVSS (Figs. 3 and 4). The ore-bearing sequence in the Zardu syncline is cut by the Koushk Fault (Fig. 5a), which trends NW-SE with a steep dip to SW (Fig. 4). The southwest block of this fault exposes shales, tuffs, and limestones. At Zardu area, within the host sequence, some sedimentary breccias and debris flow deposits are intercalated with the fine-grained ore-bearing sedimentary rocks and abruptly increase in thickness towards the southeastern part of the deposit (Fig. 5a). A rhyolitic dome, Middle Cambrian in age, intruded the ore-bearing sequence in the southeast of the deposit and several diabase dikes cut the entire ECVSS.

Mineralization

The Koushk deposit is located in the central part of the ZCB, within rocks deposited during the sag phase of the ECVSS; these include black siltstones and shales of the Koushk member that are overlain by 200 m of carbonates. The mineralization occurs as a tapering, wedge-shaped orebody within the black siltstones and shales, reaching a maximum thickness of about 111 m in the SE portion of the deposit and decreasing to less than 60 m at its northwestern limit (Fig. 5a). The Koushk orebody strikes SE−NW, with a southwesterly dip of 45°– 48°, concordant with the host rocks (Fig. 5b). In the southeastern part of the deposit, the mineralization is massive and stratabound (Rajabi et al., 2012b), although it forms a laterally continuous stratiform lens that terminates abruptly at the Koushk Fault, at its NW terminus (Fig. 5a).

Three major ore styles are distinguishable in the Koushk deposit (Fig. 5a; Rajabi et al., 2012b): (*a*) vent complex (massive sulfide ore), consisting of massive pyrite, galena, and sphalerite (Fig. 6), with minor chalcopyrite and arsenopyrite, (*b*) stockwork or feeder zone, composed of discordant stockwork style sulfide veins (Fig. 7), and (*c*) stratiform-bedded ore, including pyrite, sphalerite, and sphalerite-galena laminae, disseminated and replaced sulfides and barite (Fig. 8). There is also a poorly mineralized distal facies with banded chert, and disseminated barite and pyrite that stratigraphically overlies the stratiform ore body.

The Koushk deposit preserves well developed hydrothermal alteration of the host rocks within and around the feeder zone and vent complex, as alteration haloes that extend around these ore zones. Silicification and carbonatization (calcite, dolomite, and minor siderite) formed in association with feeder zones and vent complex, and sericitization around the feeder zone (Rajabi et al., 2012a). Carbonatization is more extensive than other alteration styles, even within the bedded ore.

Sampling and Methods

Representative samples of all mineralization styles and host rocks were collected from underground tunnels and drill cores from the Koushk deposit. The mineralogical, textural, and paragenetic analyses were carried out using reflected and transmitted light microscopy and scanning electron microscopy (SEM) at the University of Tehran, Iran, the *Universidad Nacional Autónoma de México*, Mexico, and the *Universitat de Barcelona*, Spain.

Thirty-one sulfide and eleven carbonate samples from different ore facies of the Koushk deposit were analyzed for sulfur, and oxygen-carbon stable isotope compositions, respectively (Tables 1 and 2). Sulfide and carbonate minerals were selected and separated mechanically (by

crushing and handpicking) from rock slabs following examination of thin sections to determine the primary mineralogy and purity of the areas to be sampled. Most samples were coarse enough to ensure > 98 % purity for the mineral separates. For samples that containing fine intergrowths of sphalerite, pyrite, and galena, sulfides were separated by micro-drilling directly from the polished sections under the microscope. Oxygen and carbon isotope compositions were determined for 11 carbonate samples obtained by micro-drilling.

Sulfur isotopes were analysed using a Delta C Finnigan MAT continuous-flow isotope-ratio mass spectrometer with an elemental analyzer. The isotopic analyses were carried out at the *Centres Científics i Tecnològics* of the *Universitat de Barcelona*, Spain. The results are reported in the conventional delta notation ($\delta^{34}S$) as per mil deviations from the V-CDT (Vienna Canyon Diablo Troilite) standard. The analytical precision is within ±0.1 ‰ (1σ).

Oxygen and carbon isotope compositions were determined using a Finnigan Delta Plus XL mass spectrometer with a dual inlet Gas Bench II interface at the *Instituto de Geología* of the *Universidad Nacional Autónoma de México*, Mexico. The C and O isotopic values are reported in the conventional delta notation ($\delta^{13}C$ and $\delta^{18}O$) as per mil deviations from to the V-PDB (Vienna Pee Dee Belemnite) and the V-SMOW (Vienna standard mean ocean water) compositions. The $\delta^{18}O$ values calculated for water in isotopic equilibrium with the carbonates are also reported relative to the V-SMOW standard. The instrumental precision (1σ) was calculated from 4 replicate analyses of certificated NSB-19 and LSVEC standards and was 0.5
‰ for $\delta^{13}C$ and 0.5 ‰ for $\delta^{18}O_{VSMOW}$.

Sulfide textures and paragenesis

Rajabi et al. (2012b, 2015b) interpreted the textural relations of sulfides at the Koushk and Chahmir deposits to indicate that the sulfides formed in two main stages, namely, (I) synsedimentary depositional sulfides, and (II) hydrothermal replacement mineralization. Further detailed SEM and reflected light ore microscopy reveal multiple generations of sulfide growth in the Koushk black shales and siltstones. New studies of the relationship between the sulfides and sedimentary bands represent more complex textural relationships in sulfide minerals (Fig. 9), which responds to different processes. It should be noted that hydrothermal stages at Koushk deposits probably were not discrete episodes but likely overlapped temporally.

Pyrite 1

The first generation of pyrite (py1) constitutes over 40% of all pyrite in bedded ore at Koushk deposit. It occurs as 2 to 6 μm euhedral to subhedral cubic crystals, spherical framboids, fine-grained spherulites (Fig. 10a,b,c), and tightly packed round to lenticular aggregates of polyspherulites (Fig. 10b,d) and 'bubble' textures.

Fine-grained crystalline pyrite, and framboids are a minor component of the black shales and siltstones of the Koushk member in the basin, but these types of pyrite along with spherulites are quite abundant in the bedded ore of the Koushk deposit (5–35 vol. %). Framboids consist of spherical aggregates of microcrystalline pyrite. Individual framboids are generally <2 to 7 μm in diameter and less commonly up to 15 μm in diameter.

Spherulite texture is the most common form of pyrite in the bedded ore of this deposit (Fig. 10a,c; also see Fig. 9e in Rajabi et al., 2012b) and occurs disseminated and forming laminae.

Accumulation of these spherulites, along with minor microeuhedral pyrite, makes loosely round to lenticular aggregates, called here polyspherulites (Fig. 10). Single spherulites are more common than framboids in the bedded ore; moreover, euhedral fine-grained pyrite or galena may occur at the core of some spherulites. Single spherulites are generally <2 to 7 μm in diameter and composed of radiating fibrous pyrite.

Framboids, microeuhedral and spherulite pyrites usually show close relationships and occur as random disseminations, irregular clusters, and also laminae in the bedded ore of the deposit (Fig. 10). These kinds of pyrite forms are primary kernels for subsequent pyrite growth and, are grouped into py1.

Sphalerite 1

The first generation of sphalerite (sp1, Figs. 8c-d and 10c) represents >40 percent of all sphalerite at bedded ore and commonly occurs as very fine-grained (2–20 μm) sphalerite that takes the form of irregular, elongate, and blebby fine-grained aggregates that coalesce and combine to define sphalerite-rich laminae (0.2–2 mm thick, Fig. 8c) within black shales and siltstones. Sphalerite 1 is characteristically associated with euhedral pyrite crystals, framboids and pyrite spherulites, and occurs as disseminated grains dominantly in sphalerite-pyrite rich and rarely sphalerite-galena rich laminae. At the high-grade parts of the bedded ore, sp1 occurs as laterally continuous planar laminae or as sphalerite-rich bands (Fig. 8c). These laminae or bands are separated from each other by pyrite-rich or silty laminae of the host rock.

Galena 1

Galena is a minor component of the bedded ore at the Koushk deposit. Primary (non-replacement) laminated galena (gn1) is very rare at the Koushk deposit and is commonly concentrated as very fine-grained disseminations in sphalerite-galena-rich bands (Fig. 8d). Galena also occurs as a crystalline core in some pyrite spherulites. The first stage of galena mineralization at Koushk forms fine-grained disseminated sulfide and its laminated form is very scarce.

Pyrite 2

The second generation of pyrite (py2) forms coarse anhedral to subhedral crystals aggregates, usually overgrowths on py1 in the bedded ore (Fig. 11). Subhedral crystals and coagulated aggregates of py2 displace the adjacent laminations and are more common in nodular pyrites (Fig. 11a) and around the polyspherulites (Fig. 11b-d). Considering these textures, it can be assumed that py2 nucleated on the preexisting py1, marking the diagenetic stage of the mineralization. This generation of pyrite, especially nodular pyrite, replaces carbonates (Fig. 11a) and barite (Fig. 11e,f), and is common in barren host rock bands, carbonate-rich bands, and nodules. Besides, polyspherulites show diagenetic growth in tightly packed aggregates (packed polyspherulite aggregate, PPA; Fig. 11b-d). PPAs are restricted to the banded ore facies of the deposit and usually form pyrite-rich bands.

Sphalerite 2

The second generation sphalerite (sp2) comprises about < 60 % of all sphalerite at bedded ore and locally up to 70 % in polyspherulite bands, pyrite nodules, and carbonate-rich bands or nodules (Fig. 11b-d). Sp2 consists of 10 to 100 μm crystalline aggregates that are usually associated with py2 and also occurs as variable replacement of polyspherulites, framboidal

pyrites, and disseminated barite (Fig. 11b-d). Sp2 forms late in the paragenetic sequence in the bedded ore, after the formation of pyrite nodules that displace the stage 1 phases and py2 (Figs. 9 and 11b-d).

Galena 2

The second generation of galena is a volumetrically minor phase in the bedded ore and only occurs in carbonate-rich laminae associated with stage 2 of sphalerite and pyrite. This generation of galena usually replaces carbonate nodules (Fig. 8f) and stage I of sulfides.

Pyrite 3

This generation of pyrite (py3) forms coarse-grained euhedral to subhedral crystals, and occurs as massive bodies and as vein or veinlets (Fig. 6c, d, f, g), mainly in the vent complex and the feeder zone, or as colloform pyrite around the vent complex (Fig. 6a, e). Py3 is associated with coarse-grained galena and sphalerite, and with carbonate alteration in massive high-grade accumulation of sulfides, and is a dominant sulfide phase in yellow pyrite-rich sub-facies (YPS) and pyrite-sphalerite-rich sub-facies (PSS) of the vent complex (Rajabi et al., 2012b). It also occurs in feeder zone as coarse-grained crystalline pyrite in vein and veinlets.

Galena 3

Galena 3 (gn3) is one of the main components of the vent complex, especially in the galena-sphalerite rich sub-facies (Fig. 6b, c, e, f). Coarse-grained gn3 occurs in massive bodies, in veins/veinlets, and replacements in the vent complex and feeder zone, and mainly replaces pyrite (Fig. 6e, f). This galena usually is associated with carbonatization and silicification, and along with sp3 makes the highest ore-grade mineralization in the vent complex.

Sphalerite 3

Sp3 is a common distinctive sphalerite confined to the vent complex and feeder zone, and it is indicated by coarse-grained anhedral crystals, replace pyrite and galena (Fig. 6). This type of sphalerite is commonly concentrated in the pyrite-sphalerite and galena-sphalerite rich sub-facies of the vent complex (Rajabi et al., 2012b) and veins and veinlets of the feeder zone. Sphalerite 3 replaces or overprints all other sulfide minerals associated with the mineralization (Fig 6d, e, f) and, therefore, it is the latest sulfide phase in stage III of paragenetic sequence.

Chalcopyrite and arsenopyrite

Chalcopyrite and arsenopyrite are volumetrically minor phases of the mineralization and occur throughout the vent complex. Chalcopyrite is present as fine-grained inclusions (blebs) within coarse-grained sphalerite (as chalcopyrite-disease). Arsenopyrite is scarce and occurs as fine-grained euhedral to subhedral crystals associated with galena (gn3).

Sulfur isotopes

The new sulfur isotope data for this deposit (Table 1) span the range of $\delta^{34}S$ values of previous studies (Rajabi et al., 2012b) and are most positive (Fig. 12). All the $\delta^{34}S$ values for samples from the Koushk deposit are between 6.5 and 36.7 ‰ (avg. 22.0 ‰). Significant differences in $\delta^{34}S$ values occur among different sulfide generations and ore facies.

In Koushk, the highest $\delta^{34}S$ values correspond to the bedded ore, where they vary between 9.7 and 36.7 ‰ (avg. 28.7 ‰). The $\delta^{34}S$ values from the feeder zone range between 21.8 and 26.8 ‰

(avg. 23.9 ‰), and the lowest values occur in the vent complex, between 6.5 and 24.7 ‰ (avg. 15.0 ‰).

Oxygen and carbon isotopes

The O and C isotope compositions of hydrothermal carbonates (calcite and dolomite) from the Koushk deposit are listed in Table 2. The $\delta^{18}O_{SMOW}$ values in calcite (n = 4) are between 17.1 and 19.8 ‰ (avg. 18.5 ‰) and in dolomite (n = 4) between 22.7 to 24.0 ‰ (avg. 23.5 ‰). The $\delta^{13}C_{PDB}$ values in calcite are between -8.3 and 7.0 ‰ (avg. -7.6 ‰), and in dolomite from -4.9 to -4.3 ‰ (avg. -4.6 ‰). The $\delta^{18}O_{SMOW}$ values in calcite from the host rock (Koushk member shales) in the basin (Rajabi et al., 2020) are between 18.1 and 20.5 ‰ (avg. 19 ‰) and $\delta^{13}C_{PDB}$ values are between -1.5 and 0.4 ‰ (avg. -0.3 ‰).

Discussion

Sources of sulfur

Sulfide minerals in almost all SHMS deposits show wide ranges of $\delta^{34}S$, with values from negative to highly positive (Fig. 13), especially in pyrite from carbonaceous shales hosting the sulfide mineralizations (Leach et al., 2005; Lyons et al., 2006). But, a striking feature of the Koushk deposit is the broad range (Figs. 12 and 13) of positive $\delta^{34}S$ values of sulfide minerals. This broad range of $\delta^{34}S$ values in Koushk is similar to that for other SHMS deposits worldwide (e.g., Anger et al., 1966; Goodfellow and Jonasson, 1987; Shanks et al., 1987b; Leach et al., 2005).

Seawater sulfate is considered to be the predominant source of sulfur in SHMS deposits and in other sulfide accumulations in the seafloor (Ohmoto and Goldhaber, 1997; Leach et al., 2010). Nonetheless, the processes of sulfate reduction to sulfide in different orebodies and the subsequent deposition of sulfide minerals remain controversial (Gadd et al., 2017; Magnall et al., 2016b). Thermochemical and bacterial sulfate reduction (TSR and BSR, respectively), and anaerobic oxidation of methane coupled with sulfate reduction (AOM-SR, Magnall et al., 2016b) are the most relevant processes for supplying sulfur from the seawater sulfate and deposition of sulfide minerals in SHMS deposits (e.g., Kelley et al., 2004; Shanks III, 2001, 2014; Magnall et al., 2016b; Gadd et al., 2017), discussed below in stratiform and stratabound sulfide ores.

Stratiform ore and sulfate reduction

In sulfide accumulations within marine sediments in anoxic basins, BSR is the most common geochemical mechanism for sulfide deposition; typically, it takes place under early diagenetic conditions (Goldhaber, 2003; Shanks III, 2014). Bacterial sulfate reduction occurs at temperatures of less than 110 °C (Stetter, 1999; Jørgenson et al., 1992) and results in a broad range of negative $\delta^{34}S$ values. Sulfur isotopic fractionation of BSR ranges from -20 to -60 ‰ ($\varepsilon^{34}S$, about -40 ‰ in average) relative to the parent sulfate, and that is why negative $\delta^{34}S$ values are usually obtained, diagnostic of an open system for marine sulfate (Magnall et al., 2016b; Sharp, 2017). Large ranges of $\delta^{34}S$ values can also result from a Rayleigh-type fractionation (RTF) occurring in partially closed or restricted systems (Fig. 14a), wherever marine sulfate supply is the major limiting factor (Goldhaber, 2003; Shanks III, 2014). It should also be considered that $\delta^{34}S$ values distribution also depend on other factors such as sulfate reduction rate (Leavitt et al., 2013), sulfate concentration (Habicht et al., 2002), temperature (Sagemann et

al., 1998; Sawicka et al., 2012) and content of organic-rich matter in the sediments (Goldhaber and Orr, 1995).

In the bedded ore, during the stage 1 of sulfide mineralization on/near the seafloor, temperatures could have been low enough to sustain BSR so that biogenic sulfides, as fine- grained (< 6 μm) framboidal pyrite, preserve negative $\delta^{34}S$ values (e.g., Rajabi et al., 2015a; Gadd et al., 2017). However, all $\delta^{34}S$ values from coarse framboids (> 6 μm), spherulites, galena, and diagenetic non-framboidal pyrite in the bedded ore yield high positive $\delta^{34}S$ values (from 9.7 to 32.7 ‰), revealing that the contribution of open system-BSR in the main stages of Zn-Pb mineralization is insignificant (Fig. 14b).

Framboidal pyrite in the HYC vent-distal SHMS deposit, Australia, preserves a $\varepsilon^{34}S$ of ~28 ‰ relative to the $\delta^{34}S$ value of contemporaneous seawater sulfate (Ireland et al., 2004). In the Howards Pass (HP) deposit, Yukon, Canada, a $\varepsilon^{34}S$ of ~44 ‰ is obtained from framboidal pyrite (Gadd et al., 2017). Sangster (2018) noted that these pyrite framboids are pre-exhalative and compared them with those of modern marine sedimentary open system to sulfate. Conversely, in the bedded ore of Koushk, coarse-grained framboidal and pyrite spherulites, as well as fine-grained galena, preserve a $\varepsilon^{34}S$ of ~2 ‰, which does not support this model in the deposit. In addition, S isotope analyses yield very high $\delta^{34}S$ values, up to 36.7 ‰, in stage 2 diagenetic pyrite and sphalerite (Fig. 14b, Table 1). Similarly, Strauss and Deb (unpubl. data) analyzed $\delta^{34}S_{SO4}$ in evaporites of the Ravar and Desu Series (time equivalent with ECVSS in central Iran), in the east and south of the ZCB, that range between 28 and 31 ‰ (Figs. 12, 14b). This data falls in the range of $\delta^{34}S$ values in bedded sulfides from SHMS Zn–Pb deposits of Central Iran and Early Cambrian evaporitic sulfates, suggests a common sulfur source, with small isotopic fractionation between the contemporaneous seawater sulfate and sulfides that is

not consistent with bacterial sulfate reduction (open-system BSR) that typically generates extreme shifts towards low (negative) $\delta^{34}S$ values with respect to those in the parental sulfate.

Thermochemical sulfate reduction (TSR) has been invoked as an important sulfate reduction process in the bedded ore of SHMS deposits (Alfonso et al., 2002; Ireland et al., 2004; Huston et al., 2006; Gadd et al., 2017). In this process, dissolved sulfate was a major component of metalliferous exhaled brine, that after exhalation in an anoxic basin, ponded on the seafloor and TSR occurs in the basal part of the ponded hydrothermal fluid into the bedded ore (Ireland et al., 2004; Gadd et al., 2017). Likely, such similar thermochemical sulfate reduction (TSR) by hydrothermal brines played an essential role in deposition of diagenetic sulfides of the bedded ore in the Koushk deposit (Fig. 14b).

Rather than forming via TSR, Magnall et al. (2016b) suggested that the positive $\delta^{34}S$ values in pre-ore pyrite of the bedded ore of the Tom and Jason deposits (Yukon, Canada) were generated during diagenesis. They found evidence of barite dissolution in the bedded ore, and the replacement of barite with pyrite and sphalerite with highly $\delta^{34}S$ values (range between +8 to +26 ‰). Detailed textural investigation in the bedded ore of Koushk reveals a paragenetic relationships between diagenetic sulfide mineralization and dissolution of disseminated barite in this ore facies (Fig. 11e,f). These barite grains are generally greater than 7 μm in size (up to 50 μm), which is typical of barite precipitates beneath the water-sediment interface (cf. Paytan et al., 2002; Magnall et al., 2016b), durig early diagenesis. This barite is replaced directly with all diagenetic pyrite (py2) and sphalerite (sp2), and hydrothermal sulfides of stage 2 (Fig. 11e,f). Textural evidence of barite dissolution and replacement by sulfides are commonplace in other SHMS deposits, such as Tom and Jason in Canada (Magnall et al., 2016b), carbonate-clastic hosted massive sulfide deposits as like as Red Dog in USA (Kelley et al., 2014), and Mehdiabad

(Rajabi et al., 2012a; Maghfouri et al., 2019) and Irankuh (Boveiri et al., 2017; Rajabi et al., 2019) deposits in Iran. Thus, in addition to the possible TSR process in the basal portion of the ponded hydrothermal brine (Ireland et al., 2004; Gadd et al., 2017), a significant part of diagenetic sulfides in bedded ore of the vent-proximal SHMS deposits, as well as Koushk, can achieve positive $\delta^{34}S$ values from direct replacement and dissolution of barite that formed beneath the water-sediment interface (SWI; Magnall et al., 2016b) and/or during early diagenesis (Fig. 14b).

Stratabound ore and sulfate reduction

The stratabound ore system in vent-proximal SHMS deposits includes the vent complex (massive ore) and an underlying feeder (stockwork) zone, with an alteration halo around these zones. According to the replacement ore textures and microthermometric data, the main stage of mineralization in vent-proximal SHMS deposits form from relatively high-temperature fluids. Fluid inclusion microthermometry and geochemical investigations provided evidence of a steep thermal gradient (300 to 100 °C) within the vent complexes and feeder zones in the Tom and Jason deposits in Canada (Magnall et al., 2016a). Rajabi et al. (2015b) recorded high- temperature ore-forming fluids in the vent complex of the Chahmir deposit (177 to 250 °C), Central Iran, and calculations from sphalerite-galena sulfur isotope pairs yield high temperature conditions (202 to 280 °C; using the fractionation equation by Ohmoto and Rye, 1979) in the vent complex and feeder zone of Koushk. The massive ores and mineralized feeder zones in this deposit preserve a wide range of $\delta^{34}S$ values (+3 to +26.5 ‰). Indeed, in these ore zones, these $\delta^{34}S$ values are not consistent with BSR and fluid temperatures are too high for BSR to occur. Above 110 °C (Jørgenson et al., 1992) and in the presence of organic matter as a reducing agent, sulfate can be reduced to sulfide through TSR (Fig. 14b), where smaller fractionations between

the sulfate and sulfide minerals occur under higher temperature (Kiyosu and Krouse, 1990; Magnall et al., 2016b; Sharp, 2017). In these conditions, carbonate minerals are an important by-product of TSR (Machel, 2000; 2001), which are observed in the vent complex of Koushk (Fig. 6a). Furthermore, it may be that most of the sulfate budget was consumed during TSR, in which case Rayleigh-type fractionation can also be considered (Gadd et al., 2017), in which $\delta^{34}S_{sulfide}$ values could approach the initial $\delta^{34}S$sulfate value. The $\varepsilon^{34}S$ for vent complex and feeder zone of Koushk range from 20 to 0 ‰, so if the $\delta^{34}S$ of Early Cambrian evaporites from the Ravar and Desu series is considered as sulfate source, this range of $\varepsilon^{34}S$ is compatible with TSR under high temperature (200° to 300 °C), along with high rate of sulfide deposition.

Carbon and oxygen isotopes

Both carbon and oxygen isotopic compositions of the calcite samples from the Lower Cambrian limy siltstone ($\delta^{13}C_{VPDB}$ from -1.5 to +0.4 ‰, $\delta^{18}O_{VSMOW}$ from +18.1 to +20.5 ‰) are within the range of values reported from Lower Cambrian limestones (Veizer et al., 1999), including those of Lower Cambrian carbonate rocks of the Alborz region in Iran (Kimura and Watanabe, 2001). The $\delta^{13}C_{VPDB}$ and $\delta^{18}O_{VSMOW}$ values of one sample from the Koushk member are -4.8 and +16.5 ‰, respectively, which is comparable with the reported isotopic composition
for Lower Cambrian black shales (Fig. 15a) of the Alborz region (Kimura and Watanabe, 2001).

The $\delta^{13}C$ values of hydrothermal carbonate gangue in the Koushk deposit range between -8.4 and -4.8 ‰ (Fig. 15a). The carbon isotope compositions show that the hydrothermal calcites have more negative $\delta^{13}C$ values relative to the hydrothermal dolomites, and calcite and dolomite in the alteration halo have lower $\delta^{13}C$ values relative to the host rocks (Fig. 15a). This decrease in $\delta^{13}C$

values can occur by a difference in temperature or mixing with a fluid that had a different isotopic composition (Velasco et al., 2003). The speciation of carbon in hydrothermal fluids is dependent on pH and temperature (Holmén, 2000). Bicarbonate (HCO_3^-) is the dominant species in seawater, but in acidic hydrothermal fluids, both dissolved CO_2 and HCO_3^-, could be important. The offsets for $\delta^{13}C$ at moderate to high temperature (200 to 300 °C) conditions (about 1 to 2 ‰) are small enough to be ignored for the purposes of this paper. Therefore, we did not calculate $\delta^{13}C_{CO2}$ and/or $\delta^{13}C_{HCO3^-}$ in ore fluids (Fig. 15b). All obtained $\delta^{13}C$ values fall in the range to those of $\delta^{13}C_{carbonate}$ in Early Cambrian black shales in anoxic basins (e.g., Alborz basin; Kimura and Watanabe, 2001) and $\delta^{13}C_{calcite}$ of black shales in the Chahmir area (Fig. 15 a).

The $\delta^{13}C$ values for the hydrothermal carbonates indicate a marine carbon source and reflect buffering of the fluid composition by interaction with the host sequence. Longstaffe (1989) noted that low $\delta^{13}C$ values (–30 to –9.2 ‰) for carbonates are typical of carbon derived from the decomposition of organic matter. Hence the $\delta^{13}C$ values for carbonates in the Chahmir and Koushk deposits are consistent with the $\delta^{13}C$ values of the carbonates in Early Cambrian black shales (Fig. 15a) and well below typical Cambrian marine carbonate signatures (-2 to +1 ‰: Veizer et al., 1999). Similar values are reported by Taylor et al. (2000) and Goodfellow and Jonasson (1987) for calcites in shale-hosted Zn-Pb deposits in the Belt-Purcell and Selwyn basins, respectively, in Canada.

Estimated $\delta^{18}O_{water}$ values for mineralizing fluids, based on the equations of Zheng (1999) and Horita (2014), range between +8.0 and +16.9 ‰ for the Koushk deposit (Fig. 15b). These values overlap with sedimentary rocks, and are generally compatible with basinal brines and formation water as fluid sources for this deposit (Fig. 15b). However, these $\delta^{18}O_{water}$ values for

the mineralizing fluid could represent a minor magmatic water contribution (Fig. 15b). A possible magmatic fluid contribution has also been reported for other shale-hosted Zn-Pb deposits (e.g., HYC and Lady Loretta, Australia: McGoldrick et al., 1999; Large et al., 2001), but such fluid values could also be the result of interaction between hydrothermal fluids and volcanic or pyroclastic rocks in the basin.

A genetic model for vent-proximal SHMS deposits

Rajabi et al. (2012b; 2015a,b) relied on tectono-sedimentary and textural evidence to describe the origin of the Early Cambrian SHMS deposits in Central Iran, and suggested that these deposits formed as a result of buoyant plume rising hydrothermal fluids to the seafloor (Fig. 16). More recently, other studies (Gadd et al., 2016; Magnal et al., 2016b) have revisited these genetic models for SHMS deposits and suggested diagenetic models for these deposits. But deposition of sulfide minerals and development of ore zones are different in the stratiform and stratabound orebodies. In our proposed genetic model, we investigate the development of Zn-Pb mineralization in these different ore styles of the vent-proximal SHMS deposits:

(I) *Development of stratiform ores*

(a) Deposition of fine-grained sulfides

Based on the density-temperature curves of Haas (1976) and Sangster (2002; 2018) and a few fluid inclusion data from vent-proximal SHMS deposits (e.g., Tom and Jason in Canada, Gardner and Hutcheon, 1985; Ansdell et al., 1989; Turner, 1991; Magnall et al., 2016a; Chahmir in Central Iran, Rajabi et al., 2015b), the ore-forming fluid in these deposits was slightly less dense

than seawater. When this fluid released at the seafloor, it can rise as buoyant plume (Fig. 16a), at least initially (Sato, 1972; Sangster, 2002), near and above the vent discharges. Then the ore-forming fluid is likely to be cooled by mixing with seawater, which is followed by dilution and increase in pH, therein causing rapid sulfide precipitation from the plume itself (Sangster, 2018). If the ore-forming fluid is floating over the seafloor, most metalliferous components will be dispersed by submarine currents. But in the event of a buoyant plume in a restricted environment, such as half-graben-related marine basins in Central Iran (Rajabi et al., 2015a), this fluid can settle to the seafloor after exhalation.

The hydrothermal fluid does not instantly sink into the sediments. Fluid mixing with seawater produces cooling and neutralization, and that produces destabilization of Fe, Zn, and Pb chloride complexes. In addition, the reaction between dissolved H_2S in an anoxic environment and metallic chloride complexes causes rapid precipitation of sulfides. In this extreme supersaturation conditions, the very fine-grained sulfides can originate from the brine by rapid precipitation on the seafloor (Ireland et al., 2004; Rajabi et al., 2015b; Gadd et al., 2016; 207; Yarmohammadi et al., 2016; Mahmoodi et al., 2018). This depositional model applies only for the stage 1 of sulfide mineralization, including very fine-grained framboids (< 6 μm) and euhedral crystals of py1 and maybe with minor sp1 and gn1 (Fig. 17a, c1-3), in the bedded ore of the vent-proximal SHMS deposits, as well as the vent distal ones. Although there is no isotopic data from these fine-grained sulfides in the Koushk deposit, textural evidence and isotopic data from other SHMS deposits (e.g., HYC, Ireland et al., 2004; Howard Pass, Gadd et al., 2017; Tom and Jason, Magnall et al., 2016b) suggest the role of BSR in formation of stage I fine-grained sulfides, especially at the margin of the deposit, which is characterized by lower $\delta^{34}S$ (or negative) values (Figs. 14b; 17a). Due to high precipitation rate of sulfides from the

hydrothermal brine, large aggregates of Fe components may form as precursor Fe sulfides in water column and settle on the seafloor along with silty sediments and other fine-grained sulfides. After precipitation, these precursor Fe sulfides can grow as large size pyrite framboids and spherulites or nodular aggregates.

(b) Deposition of diagenetic barite

Detailed mineralogical studies reveal the presence of disseminated barite as a minor, but important gangue mineral in bedded ore and host siltstone of the Koushk deposit (Fig. 11e). Moreover, barite-rich layers (distal facies, Fig. 5) directly overlie the sulfide mineralization. The authigenic marine precipitates as fine crystals, ranging in size from 0.5 to 5 μm (Paytan et al., 1993; 2002), but barite t Koushk is generally greater than 7 μm (ranging from 7 to 50 μm) in size, which is typical of diagenetic barite, precipitates beneath the sediment water interface (Paytan et al., 2002). Sulfide-barite replacement textures are common in the bedded ore of the Koushk deposit, which indicates that the sulfides (stage II) formed partly by replacement of preexisting barite (Fig. 11e), proposes that processes responsible for barium transport and barite deposition might have been decoupled from the Pb and Zn sulfide deposition (Magnall et al., 2016b). This replacement has also been recognized in the the Red Dog district (Alaska) (Kelley et al., 2004, b; Johnson et al., 2009) and Macmillan Pass (Magnall et al., 2016b), where textural and isotopic studies support a diagenetic origin for barite.

Advective transporting of Ba^{2+} could be in cold water, producing ‘cold-seep barites’ (Canet et al., 2014). The fundamental source of the cold-seep barium is thought to be the Ba-enriched organic matter (Magnall et al., 2016b, 2020). Such Ba-enrichment was reported from black- shales of the ECVSS in Central Iran (Rajabi et al., 2015a,b). Bacterial Sulfate reduction (diuring

early diagenesis and formation of stage I of sulfides) along with methane oxidation in the sediment pile is the suggested process for release of this biogenic barium and increase its solubility (Torres et al., 2003; Magnall et al., 2020). Carbonatization (calcite and dolomite) is the major alteration in Central Iranian SHMS deposits that show negative $\delta^{13}C$ values (Fig. 15), indicating that CO_2 produced during the oxidation of organic matter. Also, calcite nodules within the host rock of bedded ore suggests that authigenic precipitation of calcite occurred. Although biogenic and abiogenic sulfate reduction, both oxidize organic carbon and produce CO_2 (Machel, 2001; Gadd et al., 2016). Redeposition of barium, as diagenetic barite, occurs when the Ba- bearing methan-rich fluids mix with sulfate in diagenetic pore fluids (Johnson et al. 2004; Magnall et al., 2020). Association of barite with pre-ore framboidal and diagenetic pyrites, and replacement of barite with stage II of sulfides support this model for diagenetic barite formation at Koushk deposit.

(c) deposition of diagenetic sulfides

In addition to synsedimentary precipitation of sulfides, replacement processes are frequently suggested for the formation of sulfide laminae (e.g., Perkins and Bell, 1998; Eldridge et al., 1993; Polito et al., 2006). Since the reaction between metal-chloride complexes and H_2S during the formation of sulfide minerals is an acid-generating process (Anderson and Macqueen, 1982; Sangster, 2018), the pore fluids trapped during sulfide deposition between sediments and sulfides could have been slightly acidic ($Zn^{2+} + H_2S = ZnS + 2H^+$, Magnall et al., 2020), and could lead to minor carbonate dissolution and replacement by sulfide minerals (stage II; Fig 17b,$c_{7\text{-}9}$). This replacement is frequent in carbonate-rich bands and carbonate nodules of the SHMS mineralizations, as well as in the ore deposit. Replacement of carbonate by pyrite (py2) is more common than by other sulfides in bedded ore of the Koushk deposits. Although Perkins and Bell

(1998) suggested that sphalerite and galena in the HYC deposit directly replaced laminated bituminous bands, textural relationships between sulfides at the bedded ore of Koushk represent significant replacement of pyrite with diagenetic sphalerite (sp2) and minor galena (gn2) during early diagenesis. Moreover, there is widespread textural and mineralogical evidence of barite replacement by hydrothermal sulfides in the bedded ore of Koushk (Fig. 17c_5). Ultimately, this process is pervasive since it could produce sulfides (stage II) with positive $\delta^{34}S_{sulfide}$ values, formed from H_2S generated by Reductive dissolution of barite. This dissolution of barite would have caused Ba^{+2} to be remobilized upward and would have formed advancing barite fronts. The occurrence of barite-rich distal facies that directly overlies the sulfide ore (Fig. 5), suggests that barium remobilization continued through mineralization. Gadd et al. (2016; 2017) showed that multiple pyrite generations in the Howard Pass SHMS deposit, Canada, formed from mixing hydrothermal fluid and sediment pore water during sedimentation, compaction, and dewatering of unlithified sediments. The modified hydrothermal brine could still percolate through the sediment from above, react with and partially replace the preceding sulfides, barite, and carbonates, by sphalerite and galena.

(II) *Development of stratabound ores*

Development of stratabound ores, especially the vent complex, is more complicated than the bedded ore in the SHMS deposits. A continued venting of high temperature (>200 °C) ore fluids would have increased temperature of the orebody around the vent conduits. Vent complex development (VCD), along with extensive hydrothermal alteration at the top of the feeder zone of the vent-proximal SHMS deposit, took place commonly by two general processes:

(a) Brecciation and replacement of host rocks

Mineralization in the vent complex mostly depended on temperature and geochemical characteristics of hydrothermal fluids, the activity of a synsedimentary fault as a hydrothermal fluid conduit, the permeability of the host rock around the fault, and the flow of seawater circulating into the vent system. The hydrothermal fluid responsible for the main stage ore mineralization at Koushk deposit (stage III) was hot (202-280 °C). Fluid inclusion data from Chahmir deposit in Central Iran represents homogenization temperature from 170 to 226 °C at the top of the vent complex. These fluids are cooled during the ascent through the feeder conduits due to water-rock interaction, mixing with circulating seawater and diagenetic pore fluid input at the top of the vent system (Fig. 16b). This temperature drop would have been accompanied by increasing pH, and consequently by the destabilization of metal-chloride complexes. At the upper part of the feeder zone, where fluid mixing occurs close to the seafloor, by increasing the host rock permeability that strongly depends on the extent of lithification (Magnall et al., 2016a), ore-forming fluids will penetrate laterally toward the bedded ore, which leads to vent complex development into this mineralization zone.

Figures18a and 19a show the VCD through the brecciated host rock. The early hydrothermal fluids injection into the host siltstone and/or shale is associated with pervasive carbonate alteration (i.e., dolomite, siderite, and/or ankerite; Rajabi et al., 2012a, 2015b). However, the simple cooling of the fluid could not cause the carbonate to precipitate (Ohmoto, 1996), but carbonate minerals are likely to precipitate during fluid-rock interaction and increasing pH. Carbonate alteration is commonly associated with increasing permeability of the host rock and movement of ore fluids within the sediments. Magnall et al. (2016a) considered the early fluids responsible for hydrothermal alteration hotter than the late ore-forming fluids. With intensifying injection and input of relatively acidic ore-forming fluids, dissolution of rock-forming minerals

and fluid overpressure caused hydrothermal brecciation (Figs. 18a_1,a_2; 19a) and create necessary spaces for additional fluid injection and mineralization. Mineralization processes are so complicated at this stage, including dissolution of rock forming minerals, redeposition of carbonates in response to increasing pH, and redissolution of carbonates and other components due to progressive multiple fluid injection and sulfide mineralization. Quartz occurs mostly as fillings of open spaces or vein and veinlets created during the dissolution of the host rock and brecciation. Ohmoto (1996) suggested that fracturing of the host rocks in massive sulfide deposits have been caused by the high velocity of hydrothermal fluids, and that some quartz may have precipitated because of the pressure drop on fracturing.

Due to the high temperature of fluids in the vent complex, TSR was responsible for most reduced S in the hydrothermal sulfides. However, compiled data represent a range of fractionation values between sulfides and sulfate from 21 to 1 ‰ in vent complex and feeder zone of Koushk (Fig. 14). Based on Ray and Ohmoto (1974), fractionation of ≤2 would require a temperature of about 600 °C, which is not feasible in a seafloor environment (Sangster, 2018). Therefore, in addition to normal TSR, a significant part of the sulfur required to form sulfide minerals in the vent complex can be supplied by dissolution and replacement of barite by sulfide minerals and/or by a high rate of sulfate reduction at high temperatures (H-TSR). As noted before, TSR is associated with deposition of carbonate minerals, confirmed with the extensive carbonate alteration associated with stage III of sulfide mineralization in the vent complex. Colloform pyrite especially shows a close relationship with this alteration (Fig. 6a) and represents $\delta^{34}S$ similar to the coeval stage III of sulfide generation in the vent complex. Colloform pyrite is a common texture in organic-rich parts of the host rocks that were infiltrated by ore fluids in the SHMS (Fig. 18a_4). Colloform texture is commonly interpreted as evidence of

rapid sulfide precipitation into open space from a supersaturated solution (Roedder, 1968; Honjo and Sawada, 1982; Wilkinson et al., 2005). Wilkinson et al. (2005) interpreted this texture as a sulfide aggregate forms due to mixing between two fluids was the likely cause of sulfide supersaturation. The observation of such textures in the main ore stage, together with the correlation between $\delta^{34}S$ in colloform and coarse-grained euhedral pyrites (py3), are evidence of rapid precipitation of pyrite at a high degree of supersaturation and could represent fluid mixing between seawater and hydrothermal brines.

Development of a vent complex is associated with extensive sulfide replacement of barite and previous sulfides,that caused the sulfur isotope composition of the latest sulfides (stage III) exhibits a considerable overlap with former sulfide minerals. The continuous fluid injection into the vent complex leads to successive repetition of these replacement processes and development and growth of massive sulfide ore with complex textural relationships.

(b) Massive sulfide replacement in bedded ore

Part of the development of the vent complex in the SHMS deposits is the result of an extensive sulfide replacement in the bedded ore, adjacent to the vent site (Figs. 18b and 19b). This replacement can occur along prior sulfide bands or as sulfide veins mineralization among sulfide laminae and bands (Fig. 19b). If this process takes place in sulfide-poor zones of the bedded ore, development of massive ore, and vent complex will be analogous to previous processes, mentioned above, and brecciation of the host rock will be developed with replacement. But if replacement of stage 3 sulfides occurs within sulfide-rich part of the bedded ore, vent complex development will likely happen without brecciation (Figs. 18b and 19b). In this case, due to easy accessibility to sulfur for metal-rich hydrothermal fluid, the late stage of

sulfides simply replaces the former laminated and banded sulfides. Therefore, the S isotope composition in stage 3 will be too close to previous sulfides. Few non-sulfide components within the sulfide laminae are dissolved during hydrothermal fluid flow and probably are carried along with hydrothermal constituent. These dissolved components can precipitate as limited carbonatization or silicification in replacement stains or within the sulfide veins of stage 3 (Fig. $18b_{4\text{-}6}$).

Interaction of hydrothermal fluids with organic matter-rich bands will be accompanied by destructing of organic matter, thermochemical sulfate reduction and rapid precipitation of sphalerite and galena (Fig. $18b_4$). The degraded parts of organic matter (thermally altered organic matter) are carried in part along with fluids and quickly deposited in sulfide veins associated with carbonate alteration or silicification (Figs. $18b_4$; 19b).

The vent complex development (VCD) in the SHMS deposits sometimes is known as zone refining processes, which led to the growth of the massive ore and upgraded ore tenors (Rajabi et al., 2015b). Temperature-controlled replacement and VCD processes are responsible for metal zonation from the vent to the distal part of the mineralization in SHMS deposits (Lydon, 2004; Goodfellow and Lydon, 2007; Rajabi et al., 2015b).

Conclusions

An exciting feature of vent-proximal shale-hosted massive sulfide (SHMS) deposits, as Koushk in Central Iran, is the development of vent complex over the feeder zone and the preservation of sulfide mineralization with high positive $\delta^{34}S$ values. In this study, we have

recognized multiple generations of sulfides in different mineralization stages in both stratiform bedded ore and stratabound vent complex at Koushk. Detailed textural and S isotopic data from Koushk support a poor synsedimentary-exhalative model for the genesis of bedded sulfide mineralization, and indicate that vent-proximal SHMS deposits formed predominantly during the diagenesis and replacement of host rocks. This model is based on the presence of extensive diagenetic replacement of sulfide and non-sulfide minerals in the bedded ore and vent complex. A general genetic model for vent-proximal SHMS deposits can be depicted in several stages:

A) Stage 1 of mineralization includes volumetrically minor portion of ore sulfides, formed due to mixing between hydrothermal fluid and seawater, resulting in cooling and neutralization, and leads to rapid precipitation of very fine-grained sulfides, framboids (< 6 μm in size) and spherulites from the reduced water column on the seafloor in the bedded ore.

B) Interaction between descending fluids with pore fluids leads to development of diagenetic sulfide mineralization. This also could lead to carbonate and barite dissolution and replacement with stage 2 of sulfide minerals. This replacement is common in carbonate-rich bands and carbonate nodules. Evidence of barite dissolution is more common in the bedded ore, where it is associated with formation of sp2 and gn2.

C) Development of vent complex over the feeder zone is characterized by hydrothermal brecciation, and by dissolution of rock-forming minerals, earlier sulfides and barite, followed by extensive sulfide replacement, leading to deposition of stage 3 of ore sulfides. This process is associated with the replacement along prior sulfide bands or as sulfide veins mineralization among sulfide laminae and bands.

Textural relationships and S isotope data revealed that the contribution of BSR in the Zn-Pb mineralization is not so important, but the TSR, rapid sulfate reduction, and direct barite replacement could provide sufficient sulfur for main sulfide mineralization in SHMS deposits.

Acknowledgments

To memorialize one of the first author's best teachers, Donald F. Sangster, for the love and support, and for the guidance and patience in dealing with the many problems arose during this and other projects about the sediment-hosted Zn-Pb deposits of Iran, from 2007 to 2018. The *Serveis Científico-Tècnics de la Universitat de Barcelona* and the research grant 2009SGR-00444 of the *Departament d'Universitats, Recerca i Societat de la Informació (Generalitat de Catalunya)* supported sulfur isotope analyses. The *Instituto de Geofísica* and *Instituto de Geología* of the *Universidad Nacional Autónoma de México (UNAM)* supported electron microprobe analyses, which were done with the assistance of Carlos Linares, and carbon and oxygen isotopes analyses.

References

Aghanabati, A. (1998). Major sedimentary and structural units of Iran (map). Scientific Quarterly J. Geosci. 7, 29–30.

Alfonso, P., Canet, C., Melgarejo, J. C., & Fallick, A. E. (2002). Sulphur isotope composition of Silurian shale-hosted PGE-Ag-Au-Zn-Cu mineralisations of the Prades Mountains (Catalonia, Spain). Mineralium Deposita, 37(2), 198-212.

Anderson, G. M., & Macqueen, R. W. (1982). Ore Deposit models-6. Mississippi Valley-type lead-zinc deposits. Geoscience Canada, 9(2),108-117.

Anger, G., Nielson, H., Puchelt, H., & Ricke, W. (1966). Sulfur isotopes in the Rammelsberg ore deposit (Germany). Economic Geology, 61(3), 511-536.

Ansdell, K. M., Nesbitt, B. E., & Longstaffe, F. J. (1989). A fluid inclusion and stable-isotope study of the Tom Ba-Pb-Zn deposit, Yukon Territory, Canada. Economic Geology, 84(4), 841-856.

Bottrell, S.R., & Newton, R.J. (2006). Reconstruction of changes in global sulfur cycling from marine sulfate isotopes: Earth-Science Reviews, v. 75, p. 59–83.

Boveiri Konari, M., Rastad, E., & Peter, J.M. (2017). A sub-seafloor hydrothermal syn-sedimentary to early diagenetic origin for the Gushfil Zn-Pb-(Ag-Ba) deposit, south Esfahan, Iran. N. Jb. Miner. Abh. (J. Min. Geochem.) 194(1), 61–90.

Broadbent, G. C., Myers, R. E., & Wright, J. V. (1998). Geology and origin of shale-hosted Zn-Pb-Ag mineralization at the Century deposit, northwest Queensland, Australia. Economic Geology, 93(8), 1264-1294.

Canet, C., Anadón, P., González-Partida, E., Alfonso, P., Rajabi, A., Pérez-Segura, E., & Alba- Aldave, L. A. (2014). Paleozoic bedded barite deposits from Sonora (NW Mexico): Evidence for a hydrocarbon seep environment of formation. Ore Geology Reviews, 56, 292-300.

Carne, R. C., & Cathro. R. J. (1982). Sedimentary exhalative (Sedex) zinc-lead-silver deposits, northern Canadian Cordillera: Canadian Institute of Mining Bulletin, 75, 66-78.

Carr, G. R., & Smith, J. W. (1977). A comparative isotopic study of the Lady Loretta zinc-lead-silver deposit. Mineralium Deposita, 12(1), 105-110.

Chapman, L. H. (1999). Geology and genesis of the George Fisher Zn-Pb-Ag deposit, Mount Isa, Australia (Doctoral dissertation, James Cook University).

Eldridge, C. S., Williams, N., & Walshe, J. L. (1993). Sulfur isotope variability in sediment-hosted massive sulfide deposits as determined using the ion microprobe SHRIMP; II, A study of the HYC Deposit at McArthur River, Northern Territory, Australia. Economic Geology, 88(1), 1-26.

Elswick, E. R., & Maynard, J. B. (2014). Bedded barite deposits: environments of deposition, styles of mineralization, and tectonic settings.629-656.

Föerster, H., & Jafarzadeh, A. (1994). The Bafq mining district in central Iran; a highly mineralized Infracambrian volcanic field. Economic Geology, 89(8), 1697-1721.

Friedman, I., & O'Neil, J. R. (1977). Compilation of stable isotope fractionation factors of geochemical interest (Vol. 440). US Government Printing Office.

Gadd, M. G., Layton-Matthews, D., Peter, J. M., & Paradis, S. J. (2016). The world-class Howard's Pass SEDEX Zn-Pb district, Selwyn Basin, Yukon. Part I: trace element compositions of pyrite record input of hydrothermal, diagenetic, and metamorphic fluids to mineralization. Mineralium Deposita, 51(3), 319-342.

Gadd, M. G., Layton-Matthews, D., Peter, J. M., Paradis, S., & Jonasson, I. R. (2017). The world- class Howard's Pass SEDEX Zn-Pb district, Selwyn Basin, Yukon. Part II: the roles of thermochemical and bacterial sulfate reduction in metal fixation. Mineralium Deposita, 52(3), 405-419.

Gardner, H. D., & Hutcheon, I. (1985). Geochemistry, mineralogy, and geology of the Jason Pb-Zn deposits, Macmillan Pass, Yukon, Canada. Economic Geology, 80(5), 1257-1276.

Geer, K.A. (1988). Geochemistry of the stratiform zinc-lead-barite mineralization at the Meggen mine, Federal Republic of Germany: Unpublished Ph.D. thesis, Pennsylvania State University, 176 p.

Gemmell, J. B., Zantop, H., & Meinert, L. D. (1992). Genesis of the Aguilar zinc-lead-silver deposit, Argentina; contact metasomatic vs. sedimentary exhalative. Economic Geology, 87(8), 2085-2112.

Goldhaber, M. B. (2003). Sulfur-rich sediments. Treatise on Geochemistry, 7, 407.

Goldhaber, M. B., & Orr, W. L. (1995). Kinetic controls on thermochemical sulfate reduction as a source of sedimentary H_2S. Geochemical Transformations of Sedimentary Sulfur (Vairavamurthy, M. A. and Schoonen, M. A. A. eds.), ACS Symposium Series 612, 412–425. DOI:10.1021/bk-1995-0612.ch023

Goodfellow, W.D., & Jonasson, I.R. (1987). Environment of formation of the Howards Pass (XY) Zn-Pb deposits, Selwyn Basin, Yukon. In: Morin JA (ed) Mineral deposits of Northern Cordillera. Canadian Institute Mining Metallurgy, 19–50

Goodfellow, W.D., & Lydon, J.W. (2007). Sedimentary exhalative (SEDEX) deposits. Mineral deposits of Canada: a synthesis of major deposit types, district metallogeny, the evaluation of geological provinces and exploration methods (WD Goodfellow, ed.) Geol Assoc Canada, Min Dep Div, Sp Pub 5,163–183

Goodfellow, W.D., Lydon, J.W., & Turner, R.J. (1993). Geology and genesis of stratiform sediment-hosted (SEDEX) zinc-lead-silver sulphide deposits: Geological Association of Canada, Special Paper, 40, 201–252.

Gustafson, L. B., & Williams, N. (1981). Sediment-hosted stratiform deposits of copper, lead, and zinc: Economic Geology 75th Anniversary Volume, p. 139–178.

Haas Jr, J. L. (1976). Thermodynamics properties of the coexisting phases and thermochemical properties of the NaCl component in boiling NaCl solutions. US, Geol. Surv., Bull.;(United States), 1421.

Habicht, K. S., Gade, M., Thamdrup, B., Berg, P., & Canfield, D. E. (2002). Calibration of sulfate levels in the Archean ocean. Science, 298 (5602), 2372-2374.

Holmén, K. (2000). The global carbon cycle. In International Geophysics (Vol. 72, pp. 282-321). Academic Press.

Honjo, H., & Sawada, Y. (1982). Quantitative measurements on the morphology of a NH4Br dendritic crystal growth in a capillary. Journal of Crystal Growth, 58(2), 297-303.

Horita, J. (2014). Oxygen and carbon isotope fractionation in the system dolomite–water–CO2 to elevated temperatures. Geochimica et Cosmochimica Acta, 129, 111-124.

Huston, D. L., Stevens, B., Southgate, P. N., Muhling, P., & Wyborn, L. (2006). Australian Zn-Pb-Ag ore-forming systems: a review and analysis. Economic Geology, 101(6), 1117-1157.

Ireland, T., Large, R. R., McGoldrick, P., & Blake, M. (2004). Spatial distribution patterns of sulfur isotopes, nodular carbonate, and ore textures in the McArthur River (HYC) Zn-Pb-Ag deposit, Northern Territory, Australia. Economic Geology, 99(8), 1687-1709.

Johnson, C. A., Emsbo, P., Poole, F. G., & Rye, R. O. (2009). Sulfur-and oxygen-isotopes in sediment-hosted stratiform barite deposits. Geochimica et Cosmochimica Acta, 73(1), 133-147.

Johnson, C. A., Kelley, K. D., & Leach, D. L. (2004). Sulfur and oxygen isotopes in barite deposits of the western Brooks Range, Alaska, and implications for the origin of the Red Dog massive sulfide deposits. Economic Geology, 99(7), 1435-1448.

Jørgensen, B. B., Isaksen, M. F., & Jannasch, H. W. (1992). Bacterial sulfate reduction above 100 C in deep-sea hydrothermal vent sediments. Science, 258(5089), 1756-1757.

Kelley, K. D., Leach, D. L., Johnson, C. A., Clark, J. L., Fayek, M., Slack, J. F., ... & Ridley, W. I. (2004). Textural, compositional, and sulfur isotope variations of sulfide minerals in the Red Dog Zn-Pb-Ag deposits, Brooks Range, Alaska: Implications for ore formation. Economic Geology, 99(7), 1509-1532.

Kimura, H., & Watanabe, Y. (2001). Oceanic anoxia at the Precambrian-Cambrian boundary. Geology, 29(11), 995-998.

Kiyosu, Y., & Krouse, H. R. (1990). The role of organic acid in the abiogenic reduction of sulfate and the sulfur isotope effect. Geochemical Journal, 24(1), 21-27.

Large, D. E. (1983). Sediment-hosted massive sulfide lead-zinc deposits, an empirical model: Mineralog. Assoc. Canada Short Course Handbook, v. 8, p. 1-30.

Large, D., & Walcher, E. (1999). The Rammelsberg massive sulphide Cu-Zn-Pb-Ba-Deposit, Germany: an example of sediment-hosted, massive sulphide mineralisation. Mineralium Deposita, 34(5-6), 522-538.

Large, R. R., Bull, S. W., & Winefield, P. R. (2001). Carbon and oxygen isotope halo in carbonates related to the McArthur River (HYC) Zn-Pb-Ag deposit, north Australia: Implications for sedimentation, ore genesis, and mineral exploration. Economic Geology, 96(7), 1567-1593.

Large, R. R., Bull, S. W., Cooke, D. R., & McGoldrick, P. J. (1998). A genetic model for the HYC Deposit, Australia; based on regional sedimentology, geochemistry, and sulfide-sediment relationships. Economic Geology, 93(8), 1345-1368.

Leach D.L., Sangster, D.F., Kelley, K.D., Large, R.R., Garven, G., Allen, C.R., Gutzmer, J., & Walters, S. (2005). Sediment-hosted lead-zinc deposits: Aglobal perspective. Economic Geology, 100, 561-607.

Leach, D. L., Bradley, D. C., Huston, D., Pisarevsky, S. A., Taylor, R. D., & Gardoll, S. J. (2010). Sediment-hosted lead-zinc deposits in Earth history. Economic Geology, 105(3), 593-625.

Leavitt, W. D., Halevy, I., Bradley, A. S., & Johnston, D. T. (2013). Influence of sulfate reduction rates on the Phanerozoic sulfur isotope record. Proceedings of the National Academy of Sciences, 110(28), 11244-11249.

Longstaffe, F.J. (1989). Stable isotopes as tracers in clastic diagenesis. In: Burial Diagenesis, I.E. Hutcheon, ed., Mineralogical Association of Canada Short Course, Volume 15, 201–277.

Lydon, J. W. (2004). Genetic Models for Sullivan and other Sediment Hosted Lead-Zinc Sulphide Deposits. Deb, M., Goodfellow, W. D. (eds) Sediment-hosted lead-zinc sulphide deposits: attributes and models of some major deposits in India, Australia and Canada, p. 149-190

Lyons, T. W., Gellatly, A. M., McGoldrick, P. J., & Kah, L. C. (2006). Proterozoic sedimentary exhalative (SEDEX) deposits and links to evolving global ocean chemistry. Memoir of the Geological Society of America 198:169-1841198

Machel, H. G. (2000). Thermochemical sulfate reduction in the Devonian Nisku Formation, Alberta, Canada–a unique sour gas play with generally applicable characteristics. American Association of Petroleum Geologists Bulletin, 84, 1395-1518.

Machel, H. G. (2001). Bacterial and thermochemical sulfate reduction in diagenetic settings—old and new insights. Sedimentary Geology, 140(1-2), 143-175.

Maghfouri, S., Hosseinzadeh, M. R., Choulet, F., Alfonso, P., Zadeh, A. M. A., & Rajabi, A. (2019). Vent-proximal sub-seafloor replacement clastic-carbonate hosted SEDEX-type mineralization in the Mehdiabad world-class Zn-Pb-Ba-(Cu-Ag) deposit, Southern Yazd Basin, Iran. Ore Geology Reviews, 113, 103047.

Magnall, J. M., Gleeson, S. A., & Paradis, S. (2020). A new subseafloor replacement model for the macmillan pass clastic-dominant Zn-Pb±Ba deposits (Yukon, Canada). Economic Geology.

Magnall, J. M., Gleeson, S. A., Blamey, N. J. F., Paradis, S., & Luo, Y. (2016a). The thermal and chemical evolution of hydrothermal vent fluids in shale hosted massive sulphide (SHMS) systems from the MacMillan Pass district (Yukon, Canada). Geochimica et Cosmochimica Acta, 193, 251-273.

Magnall, J. M., Gleeson, S. A., Stern, R. A., Newton, R. J., Poulton, S. W., & Paradis, S. (2016b). Open system sulphate reduction in a diagenetic environment–Isotopic analysis of barite (δ34S and δ18O) and pyrite (δ34S) from the Tom and Jason Late Devonian Zn–Pb–Ba deposits, Selwyn Basin, Canada. Geochimica et Cosmochimica Acta, 180, 146-163.

Mahmoodi, P., Rastad, E., Rajabi, A., & Peter, J. M. (2018). Ore facies, mineral chemical and fluid inclusion characteristics of the Hossein-Abad and Western Haft-Savaran sediment-hosted Zn-Pb deposits, Arak Mining District, Iran. Ore Geology Reviews, 95, 342-365.

Mahmoodi, P., Rastad, E., Rajabi, A., Alfonso, P., Canet, C., & Peter, J.M. (2020) Genetic model for the Jurassic shale-hosted Zn-Pb deposits, Malayer-Esfahan Metallogenic Belt: insight on stable isotope geochemistry in combination with sedimentology and textural characteristics. Journal of Geochemical Exploration (submitted)

McClay, K.R., & Bidwell, G.E. (1986). Geology of the Tom deposit, Macmillan Pass, Yukon: Canadian Institute of Mining and Metallurgy Special Volume 37, p. 100–114.

McGoldrick, P. J., Dunster, J., & Aheimer, M. (1999). New sedimentological, geochemical and textural observations from the Lady Loretta deposit: Implications for ore genesis. Basins, fluids and Zn-Pb ores: Hobart, Australia, Centre for Ore Deposit Research, CODES Special Publication, 2, 49-58.

Movahednia, M., Rastad, E., Rajabi, A., Gonzalez, F.J., Alfonso, P., Choulet, F., & Canet, C. (2020). The Ab-Bagh Late Jurassic-Early Cretaceous sediment-hosted Zn-Pb deposit, Sannandaj-Sirjan Zone, Iran. Ore Geology Reviews, 103484.

Ohmoto, H. (1996). Formation of volcanogenic massive sulfide deposits: the Kuroko perspective. Ore geology reviews, 10(3-6), 135-177.

Ohmoto, H., & Goldhaber, M.B. (1997). Sulfur and carbon isotopes. In: Barnes, H.L. (ed.), Geochemistry of Hydrothermal Ore Deposits, 3rd ed. Wiley, New York, pp. 517–611.

Ohmoto, H., & Rye, R. O. (1979). Isotopes of sulfur and carbon. in ‘‘Geochemistry of hydrothermal ore deposits’’, HL Barnes ed.509-567

Painter, M. G., Golding, S. D., Hannan, K. W., & Neudert, M. K. (1999). Sedimentologic, petrographic, and sulfur isotope constraints on fine-grained pyrite formation at Mount Isa Mine and environs, Northwest Queensland, Australia. Economic Geology, 94 (6), 883-912.

Paytan, A., Kastner, M., Martin, E.E., Macdougall, J.D., & Herbert, T., 1993, Marine barite as a monitor of seawater strontium isotope composition: Nature, 366, 445–449.

Paytan, A., Mearon, S., Cobb, K., & Kastner, M. (2002). Origin of marine barite deposits: Sr and S isotope characterization. Geology, 30(8), 747-750.

Perkins, W. G., & Bell, T. H. (1998). Stratiform replacement lead-zinc deposits; a comparison between Mount Isa, Hilton, and McArthur River. Economic Geology, 93(8), 1190-1212.

Polito, P. A., Kyser, T. K., Golding, S. D., & Southgate, P. N. (2006). Zinc deposits and related mineralization of the Burketown mineral field, including the world-class Century deposit, northern Australia: Fluid inclusion and stable isotope evidence for basin fluid sources. Economic Geology, 101(6), 1251-1273.

Rajabi, A., Canet, C., Rastad, E., & Alfonso, P. (2015a). Basin evolution and stratigraphic correlation of sedimentary-exhalative Zn–Pb deposits of the Early Cambrian Zarigan–Chahmir Basin, Central Iran. Ore Geology Reviews, 64, 328-353.

Rajabi, A., Mahmoodi, P., Rastad, E., Niroomand, S., Canet, C., Alfonso, P., Tabakh Shabani, A., & Yarmohammadi, A. (2019). Comments on "Dehydration of hot oceanic slab at depth 30–50 km: Key to formation of Irankuh-Emarat Pb-Zn MVT belt, Central Iran" by Mohammad Hassan Karimpour and Martiya Sadeghi. Journal of Geochemical Exploration, 205, 106346

Rajabi, A., Rastad, E., & Canet, C. (2012a). Metallogeny of Cretaceous carbonate-hosted Zn–Pb deposits of Iran: geotectonic setting and data integration for future mineral exploration. International Geology Review, 54(14), 1649-1672.

Rajabi, A., Rastad, E., Alfonso, P., & Canet, C. (2012b). Geology, ore facies and sulphur isotopes of the Koushk vent-proximal sedimentary-exhalative deposit, Posht-e-Badam block, Central Iran. International Geology Review, 54(14), 1635-1648.

Rajabi, A., Rastad, E., Canet, C., & Alfonso, P. (2015b). The early Cambrian Chahmir shale-hosted Zn–Pb deposit, Central Iran: an example of vent-proximal SEDEX mineralization. Mineralium Deposita, 50(5), 571-590.

Ramezani, J., & Tucker, R. D. (2003). The Saghand region, central Iran: U-Pb geochronology, petrogenesis and implications for Gondwana tectonics. American Journal of Science, 303(7), 622-665.

Roedder, E. (1968). The non-colloidal origin of' colloform textures in sphalerite ores. Economic Geology, 63(5), 451-471.

Rushdi, A. I., McManus, J., & Collier, R. W. (2000). Marine barite and celestite saturation in seawater. Marine Chemistry, 69(1-2), 19-31.

Rye, R. O., & Ohmoto, H. (1974). Sulfur and carbon isotopes and ore genesis: a review. Economic Geology, 69(6), 826-842.

Sagemann, J., Jørgensen, B. B., & Greeff, O. (1998). Temperature dependence and rates of sulfate reduction in cold sediments of Svalbard, Arctic Ocean. Geomicrobiology Journal, 15(2), 85-100.

Sangster, D. F. (2002). The role of dense brines in the formation of vent-distal sedimentary-exhalative (SEDEX) lead–zinc deposits: field and laboratory evidence. Mineralium Deposita, 37(2), 149-157.

Sangster, D. F. (2018). Toward an integrated genetic model for vent-distal SEDEX deposits. Mineralium Deposita, 53(4), 509-527.

Sato, T. (1972). Behaviours of ore-forming solutions in seawater: Mining Geology, 22:31–42

Sawicka, J. E., Jørgensen, B. B., & Brüchert, V. (2012). Temperature characteristics of bacterial sulfate reduction in continental shelf and slope sediments. Biogeosciences, 9(8), 3425.

Scott, K. M., Smith, J. W., Sun, S. S., & Taylor, G. F. (1985). Proterozoic copper deposits in NW Queensland, Australia: Sulfur isotopic data. Mineralium Deposita, 20(2), 116-126.

Shanks III, W. C. (2001). Stable isotopes in seafloor hydrothermal systems: vent fluids, hydrothermal deposits, hydrothermal alteration, and microbial processes. Reviews in Mineralogy and Geochemistry, 43(1), 469-525.

Shanks III, W. P. (2014). Stable Isotope Geochemistry of Mineral Deposits. Treatise on Geochemistry 2nd Edition, 13, 59-85.

Shanks, W. C., & Seyfried, W. E. (1987a). Stable isotope studies of vent fluids and chimney minerals, southern Juan de Fuca Ridge: Sodium metasomatism and seawater sulfate reduction. Journal of Geophysical Research: Solid Earth, 92(B11), 11387-11399.

Shanks, W. C., Woodruff, L. G., Jilson, G. A., Jennings, D. S., Modene, J. S., & Ryan, B. D. (1987b). Sulfur and lead isotope studies of stratiform Zn-Pb-Ag deposits, Anvil Range, Yukon; basinal brine exhalation and anoxic bottom-water mixing. Economic Geology, 82(3), 600-634.

Sharp, Z. (2017). "Principles of Stable Isotope Geochemistry, 2nd Edition. doi: 10.5072/FK2GB24S9F

Smith, J. W., Burns, M. S., & Croxford, N. J. W. (1978). Stable isotope studies of the origins of mineralization at Mount Isa. I. Mineralium Deposita, 13(3), 369-381.

Stetter, K. O. (1999). Extremophiles and their adaptation to hot environments. FEBS letters, 452(1-2), 22-25.

Stosch, H., Romer, R., Daliran, F. and Rhede, D. (2011). Uranium–lead ages of apatite from iron oxide ores of the Bafq District, East-Central Iran: Mineralium Deposita, 46, 9–21.

Taylor, B. E., & Beaudoin, G. (2000). Sulphur isotope stratigraphy of the Sullivan Pb-Zn-Ag deposit, BC: Evidence for hydrothermal sulphur, and bacterial and thermochemical sulphate reduction. Geological Association of Canada, Mineral Deposits Division, 696-719.

Taylor, B.E., Leitch, C.H.B., Turner, R.J.W., & Watanabe, D.H. (2000). Oxygen and hydrogen isotope evidence for the origins of mineralizing and alteration fluids at the Sullivan Pb–Zn–Ag mine and vicinity, Kimberley, British Columbia, in Lydon, T., Hoy, T., Slack, J.F. and Knapp, M., eds., The Sullivan Deposit and its Geological Environment: Special Publication 1, Mineral Deposits Division of the Geological Association of Canada, St. John's, Newfoundland, p. 652–672.

Torres, M. E., Bohrmann, G., Dubé, T. E., & Poole, F. G. (2003). Formation of modern and Paleozoic stratiform barite at cold methane seeps on continental margins. Geology, 31(10), 897-900.

Turner R. J. (1991). Jason stratiform Zn-Pb-barite deposit, Selwyn Basin, Canada (NTS 105-0-1): geological setting, hydrothermal facies and genesis (eds. J. G. Abbott and R. J. Turner). Geological Survey of Canada Open File 2169, pp. 137–175.

Veizer, J., Ala, D., Azmy, K., Bruckschen, P., Buhl, D., Bruhn, F. & Jasper, T. (1999). 87Sr/86Sr, $\delta^{13}C$ and $\delta^{18}O$ evolution of Phanerozoic seawater. Chemical Geology, 161(1-3), 59-88.

Velasco, F., Herrero, J. M., Yusta, I., Alonso, J. A., Seebold, I., & Leach, D. (2003). Geology and geochemistry of the Reocín zinc-lead deposit, Basque-Cantabrian basin, northern Spain. Economic Geology, 98(7), 1371-1396.

Whelan, J. F., Rye, R. O., & deLorraine, W. F. (1984). The Balmat-Edwards zinc-lead deposits; synsedimentary ore from Mississippi Valley-type fluids. Economic Geology, 79(2), 239-265.

Wilkinson, J. J., Eyre, S. L., & Boyce, A. J. (2005). Ore-forming processes in Irish-type carbonate-hosted Zn-Pb deposits: Evidence from mineralogy, chemistry, and isotopic composition of sulfides at the Lisheen mine. Economic Geology, 100(1), 63-86.

Yarmohammadi, A., Rastad, E., & Rajabi, A. (2016). Geochemistry, fluid inclusion study and genesis of the sediment-hosted Zn-Pb (±Ag±Cu) deposits of the Tiran basin, NW of Esfahan, Iran. Neues Jahrbuch für Mineralogie-Abhandlungen: Journal of Mineralogy and Geochemistry, 193(2), 183-203.

Zheng, Y. F. (1999). Oxygen isotope fractionation in carbonate and sulfate minerals. Geochemical Journal, 33(2), 109-126.

Table Captions

Table 1: Sulfur isotope data for various sulfides of the Koushk deposit.

Table 2: Carbon and oxygen isotope data for carbonate mineral separates and whole rocks of the Koushk deposit. Also shown are calculated values for fluids in equilibrium with the carbonates, given a temperature determined by S isotope geochemistry.

Figure captions:

Fig. 1: a) Simplified tectonic map of Iran (modified after Aghanabati, 1998; Rajabi et al., 2019) showing the location of the Zarigan–Chahmir basin (yellow outlined box labeled (b)) in the Posht-e-Badam block. **b**) Lithotectonic shaded relief map representing the main faults of the Posht-e-Badam block. The Zarigan–Chahmir basin (ZCB) is marked by the Early Cambrian volcano-sedimentary sequence (ECVSS) that hosts the shale-hosted Zn–Pb deposits of Central Iran (Rajabi et al., 2012b, 2015a).

Fig. 2: Simplified geological map of the Posht-e-Badam block (between Yazd block on the left and Tabas block on the right); and Zarigan–Chahmir basin (ZCB), showing locations of the SHMS deposits (modified after Rajabi et al., 2015a). CF: Chapedony Fault, KbF: Kuhbanan Fault, KF: Kalmard Fault, NF: Naeini Fault, PF: Posht-e-Badam Fault.

Fig. 3: Lithostratigraphic correlation diagram of the Early Cambrian volcano-sedimentary sequence (ECVSS) in the Zarigan–Chahmir basin showing the stratigraphic position of the mineral deposits (after Rajabi et al., 2015a).

Fig. 4: Geological map of the Koushk deposit and a SW–NE cross-section of the deposit. The Zardu and Pahnu mining zones include the main ore body (modified after Rajabi et al., 2012b).

Fig. 5: a) Plan view of the ore sequence and different ore facies in the Koushk deposit, 940 mining level (Rajabi et al., 2012b). **b**) Geological cross section (A-B in Fig. 5a) from the bedded ore of the Koushk deposit (modified after Koushk mining company).

Fig. 6: Hand specimen (**a-d**) and microscopic (**e-g**) photographs of vent complex, Koushk deposit. **a**) massive colloform pyrite (py3) mineralization around the organic matter (om), within a carbonate (ca) matrix. **b** and **c**) heterogeneous massive sulfide texture consisting of pyrite (py3), sphalerite (sp3), galena (gn3), and quartz (qz) in brecciated black siltstone (si). **d**) massive pyrite (py3) and sphalerite (sp3) ore in which pyrite was replaced with sphalerite. **e-f**) Replacement of pyrite with galena and sphalerite in vent complex, followed by replacement of galena with sphalerite. (qz: quartz, ca: carbonate, si: siltstone)

Fig. 7: Hand specimen (**a-e**) and microscopic (**f-l**) photographs of the feeder (stockwork) zone. **a** and **b**) sulfide mineralization in quartz and carbonate veins and veinlets within brecciated siltstones (si). **c-d**) sulfide veinlets and intense in altered black siltstone (si) and quartz (qz) veining. **f-h**) galena (gn3) and sphalerite (sp3) veins of the feeder zone, associated with coarse- grained pyrite (py3). **i-k**) Complex replacement textures between sulfide minerals in feeder zone. Replacement of pyrite with galena and sphalerite is shown. In addition, galena was replaced with sphalerite. (qz: quartz, ca: carbonate, si: siltstone)

Fig. 8: Hand specimen (**a-c**) and reflected light microscopic (**e-g**) photographs of the bedded ore mineralization. **a**) Very fine lamination of pyrite in black siltstone and carbonaceous shale. **b**)

Detrital clast within sulfide laminae of bedded ore and load cast structure under the clast (white arrow). **c**) Laminated pyrite and sphalerite-rich silty band within high-grade bedded ore. Black arrow represents replacement of carbonate (calcite) by diagenetic pyrite (py2). **d** and **e**) Detail of pyrite laminae and disseminated sphalerite (sp1) and galena (gn1), showing variably sharp and diffuse edges to pyrite-rich laminae. **f**) replacement of carbonate nodule with galena (gn2). Om: organic matter, py: pyrite, sp: sphalerite, gn: galena.

Fig. 9: Mineral association different ore stages of the Koushk deposit

Fig. 10: Reflected light photomicrographs of pyrite in bedded ore. **a**) framboidal and spherulite pyrite (py1) intergrown with sphalerite (sp1); **b**) polyspherulite aggregate of pyrite (py1) and disseminated sphalerite (sp1) in host siltstone. **c**) spherulite pyrite and fine-grained sphalerite (sp1). **d**) polyspherulites and diagenetic tightly packed polyspherulites aggregates (PPA).

Fig. 11: Nodular carbonates and stage II sulfides. **a**) replacement of coarse py2 clot in a calcite nodule (c), **b**-**d**) replacement of packed polyspherulite aggregates (PPA) of py2 with diagenetic sphalerite (sp2). **e**-**f**) replacement of diagenetic barite (ba) with stage II of sulfides (s).

Fig. 12: Histogram of $\delta^{34}S$ values of sulfides from the Koushk deposit. py: pyrite, gn: galena, sp: sphalerite. Numbers indicate sulfide generations (see Fig. 9). Sulfur isotope composition of seawater sulfate (Bottrell and Newton, 2006)

Fig. 13: Distribution of sulfur isotope compositions for sulfide minerals from selected SHMS deposits. Sulfur isotope composition of seawater sulfate (Bottrell and Newton, 2006)

Fig. 14: a) A schematic of closed-system, Rayleigh-type fractionation (RTF) of sulfur isotopes during bacterial sulfate reduction ($\varepsilon^{34}S \approx 40$ ‰). The solid red and green lines show the

evolution in $\delta^{34}S$ values of sulfate and sulfide, respectively, in RTF; the dashed blue line represents the $\delta^{34}S$ value of total accumulated sulfide, which reaches the initial $\delta^{34}S$ value of sulfate when no sulfate remains (from Magnall et al., 2016a). **b**) possible sulfate reduction systems in different sulfide generations of the vent-proximal Koushk SHMS deposit. There is no isotopic data from the stage 1 of sulfide mineralization at Koushk deposit, and the possible range is suggested based on textural evidence and isotopic studies on these types of sulfides in other SHMS deposits (e.g., Tom and Jason, Magnall et al., 2016a; Howard's Pass Zn-Pb district, Gadd et al., 2016)

Fig. 15: Bivariate plot of $\delta^{13}C$ versus $\delta^{18}O$ values for hydrothermal carbonate gangue, host rock and Early Cambrian carbonate samples from the Koushk deposit. Data from: Sources of data are as follows: Mahmoodi et al., 2020 (Hosseinabad and Haftsavaran deposits); Ansdell et al. 1989 (Tom deposit); Taylor et al., 2000 (Sullivan deposit); Large et al., 1998 (HYC deposit); Kimura and Watanabe, 2001 (Early Cambrian black shales); Sharp, 2017 (sedimentary rocks; MVT ore fluids).

Fig. 16: A schematic 3D model of the vent-proximal SHMS (SEDEX) mineralizations. Because the ore-forming fluid of the Central Iranian SHMS deposit was to a small degree less dense than seawater (Rajabi et al., 2015b), when it was released at the seafloor, it rose as a buoyant plume, at least initially, above the fluid vent, then with mixing and cooling, it can settle to the seafloor after exhalation. **a**) deposition of the early stage of sulfides in bedded ore. **b**) vent complex development (VCD). Numbers and black rectangular represent sample locations and genetic processes: **(1)** figure 17, **(2)** Figures 18a and 19a, **(3)** Figures 18b and 19b.

Fig. 17: A schematic representation of the proposed genetic model for development of stratiform ores in vent-proximal Koushk SHMS deposit (no scale implied) and textural evidence for the model. Adapted and modified from Ireland et al. (2004), Magnall et al. (2016b) and Gadd et al. (2017). **a**) Synsedimentary to very early diagenesis fine-grained sulfide (stage I) deposition. **b**) Sinking and percolating of brine into permeable muds, followed by replacement of carbonate nodules, barite and preexisting (stage I) sulfides with precipitate diagenetic sulfide (stage II, py2, sp2, and gn2). c) Reflected light photomicrographs and SEM-BSE images from sulfide mineralization in bedded ore: (**1**) laminated framboids and spherulite pyrite, (**2**) spherulite pyrite intergrowth with sphalerite, (**3**) BSE image of spherulites. Galena occurs at the core of the spherulite aggregates of pyrite, (**4**) pyrite nodules (black arrows) in laminated pyritic siltstone, (**5** & **6**) replacement of barite (ba) by diagenetic sulfides (stage II), indicated with blue arrow, (**7** & **8**) replacement of packed polyspherulite aggregates (PPAs) with sphalerite (sp2), (**9**) replacement of barite and carbonate nodule with sphalerite (sp2) and galena (gn2).

Fig. 18: Vent complex development (VCD) process within different parallel dissections of a sample from of the vent complex boundaries with feeder zone (a, Koushk deposit) and bedded ore, showing brecciation, alteration, and massive replacement in. **a**) Brecciation and replacement of host rocks (samples from Koushk deposit). **b**) Massive sulfide replacement in bedded ore (samples from Chahmir deposit). See Fig. 16 for the location of samples in a schematic model of the vent-proximal SHMS deposits.

Fig. 19: A schematic representation of vent complex development (VCD) and massive sulfide replacement in vent-proximal SHMS deposits. **a**) Brecciation and replacement of sulfides in altered host rocks, **b**) Massive sulfide replacement in laminated sulfides of the bedded ore, adjacent to the vent complex. See the text for more explanation.

No	Sample	Mineral	Ore facies	Mineral symbol	$\delta^{34}S$	No	Sample	Mineral	Ore facies	Mineral symbol	$\delta^{34}S$
1	K-Bg*	Sphalerite	Bedded Ore	sp2	23.8	**17**	K-3-1	Colloform Pyrite	Vent Complex	py2	16.7
2	Zr-7*	Sphalerite	Bedded Ore	sp2	23.9	**18**	K-3-4	Pyrite	Vent Complex	py3	15.8
3	K-P1*	Pyrite	Bedded Ore	py2	36.7	**19**	K 4a	Pyrite	Bedded ore	py2	29.4
4	K-P2*	Pyrite	Bedded Ore	py2	34.5	**20**	K 5 e1	Pyrite	Feeder	py3	26.8
5	K-BP*	Pyrite	Bedded Ore	py2	31.4	**21**	K 5 e2	Sphalerite	Feeder	sp3	23.5
6	K-G2*	Galena	Vent Complex	ga3	17.0	**22**	K 6a1	Pyrite	Bedded ore	py2	32.7
7	K-GV1*	Galena	Vent Complex	ga3	16.7	**23**	K 6-5	Pyrite	Bedded ore	py2	27.9
8	K-GS1*	Galena	Vent Complex	ga3	17.8	**24**	K6-e8	Pyrite	Bedded ore	py2	31.9
9	K-VS1*	Sphalerite	Vent Complex	sp3	6.7	**25**	K-1-6	Galena	Feeder Zone	ga3	21.8
10	K-VS2*	Sphalerite	Vent Complex	sp3	6.5	**26**	K-1-7	Sphalerite	Vent Complex	sp3	23.8
11	K-VP*	Pyrite	Vent Complex	py3	11.7	**27**	K-1-13	Sphalerite	Vent Complex	sp3	24.7
12	F-GL*	Galena	Feeder Zone	ga3	21.8	**28**	K-1-14	Galena	Vent Complex	ga3	22.3
13	F-SL*	Sphalerite	Feeder Zone	sp3	25.1	**29**	K-2-1	Galena	Vent Complex	ga3	8.3
14	F-S2*	Sphalerite	Feeder Zone	sp3	24.2	**30**	K-2-2	Sphalerite	Vent Complex	sp3	7.1
15	K4-GN	Galena	Bedded ore	gn2	30.6	**31**	K6py	Pyrite	Bedded ore	py2	32.4
16	CK4	Pyrite	Bedded ore	py2	9.7						

***** Data from Rajabi et al. (2012b)

Sample	Mineral	Description	Measure (‰)	Calculated $\delta^{18}O_{VSMOW}$ (‰)

						water composition at T (°C)			
			$\delta^{13}C_{VPDB}$	$\delta^{18}O_{VPDB}$	$\delta^{18}O_{VSMOW}$	200	250	280	1000 lnα
1	Calcite	Hydrothermal alteration in vent complex	-7.0	-13.0	17.5	8.4	10.3	11.8	**a**
2	Calcite		-8.3	-10.9	19.7	10.6	12.5	14.0	
3	Calcite		-7.9	-10.8	19.8	10.7	12.6	14.1	
4	Calcite		-7.2	-13.4	17.1	8.0	9.9	11.4	
5	Dolomite		-4.6	-7.1	23.6	12.7	14.8	16.5	**b**
6	Dolomite		-4.9	-6.9	23.8	12.9	15.0	16.7	
7	Dolomite		-4.3	-8.0	22.7	11.8	13.9	15.6	
8	Dolomite		-4.7	-6.7	24.0	13.1	15.2	16.9	
9	Calcite	Black Shale	-4.8	-13.9	16.5	-	-	-	-
10	Calcite	Silty limestone (Koushk member)	0.4	-10.1	20.5	-	-	-	-
11	Limestone	Upper carbonate member	0.2	-9.0	21.6	-	-	-	-

Notes: $\delta^{18}O_{SMOW} = 1.03086 \times \delta^{18}O_{PDB} + 30.86$ (Friedman and O'Neil, 1977)

a) $1000 \ln (\text{calcite-}H_2O) = (4.010\times 10^6/T^2) - (4.660\times 10^3/T) + 1.710$ (Zheng, 1999)

b) $1000 \ln (\text{dolomite-}H_2O) = (3.140\times 10^6/T^2) + -3.140$ (Horita, 2014)

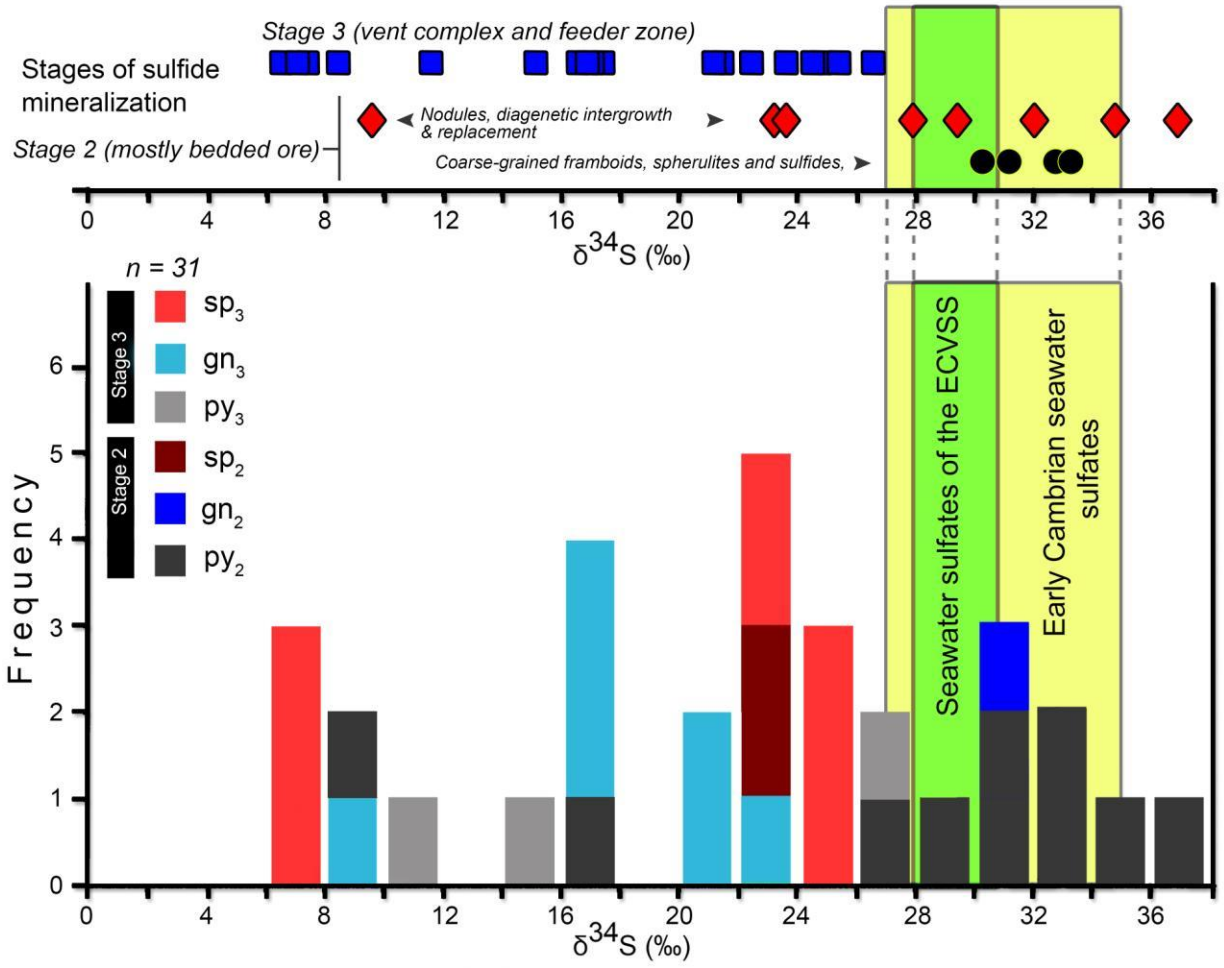

Posisble sulfate reduction systems in vent-proximal SHMS deposit (e.g., Koushk)

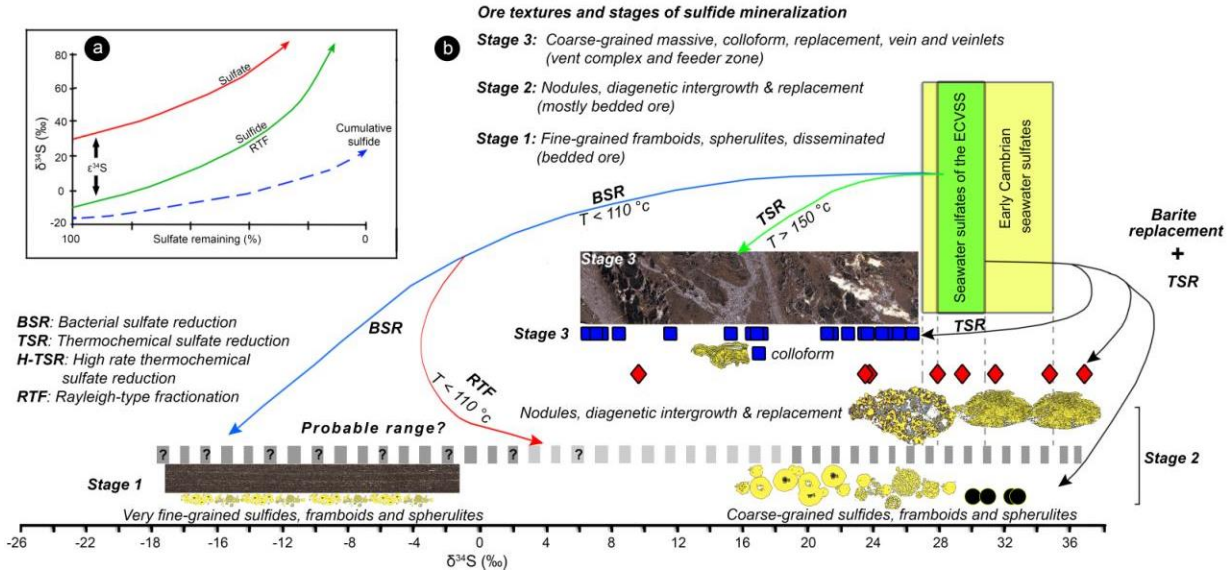

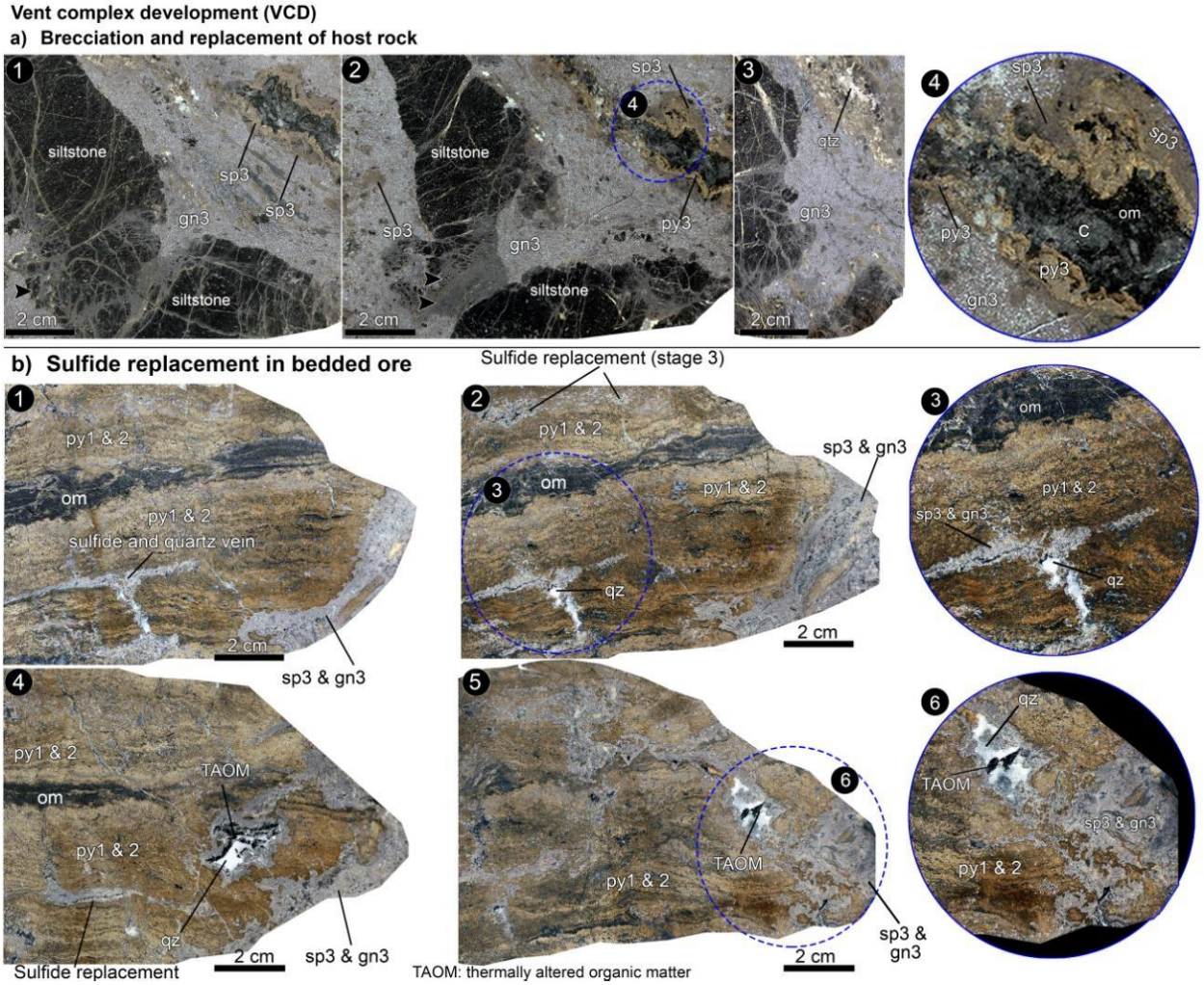
Vent complex development (VCD)
a) Brecciation and replacement of host rock
siltstone
sp3
gn3
2 cm
py3
qtz
om
c
b) Sulfide replacement in bedded ore
Sulfide replacement (stage 3)
py1 & 2
sulfide and quartz vein
sp3 & gn3
qz
TAOM
Sulfide replacement
TAOM: thermally altered organic matter

Vent complex development (VCD) and massive replacement ore in SHMS deposits

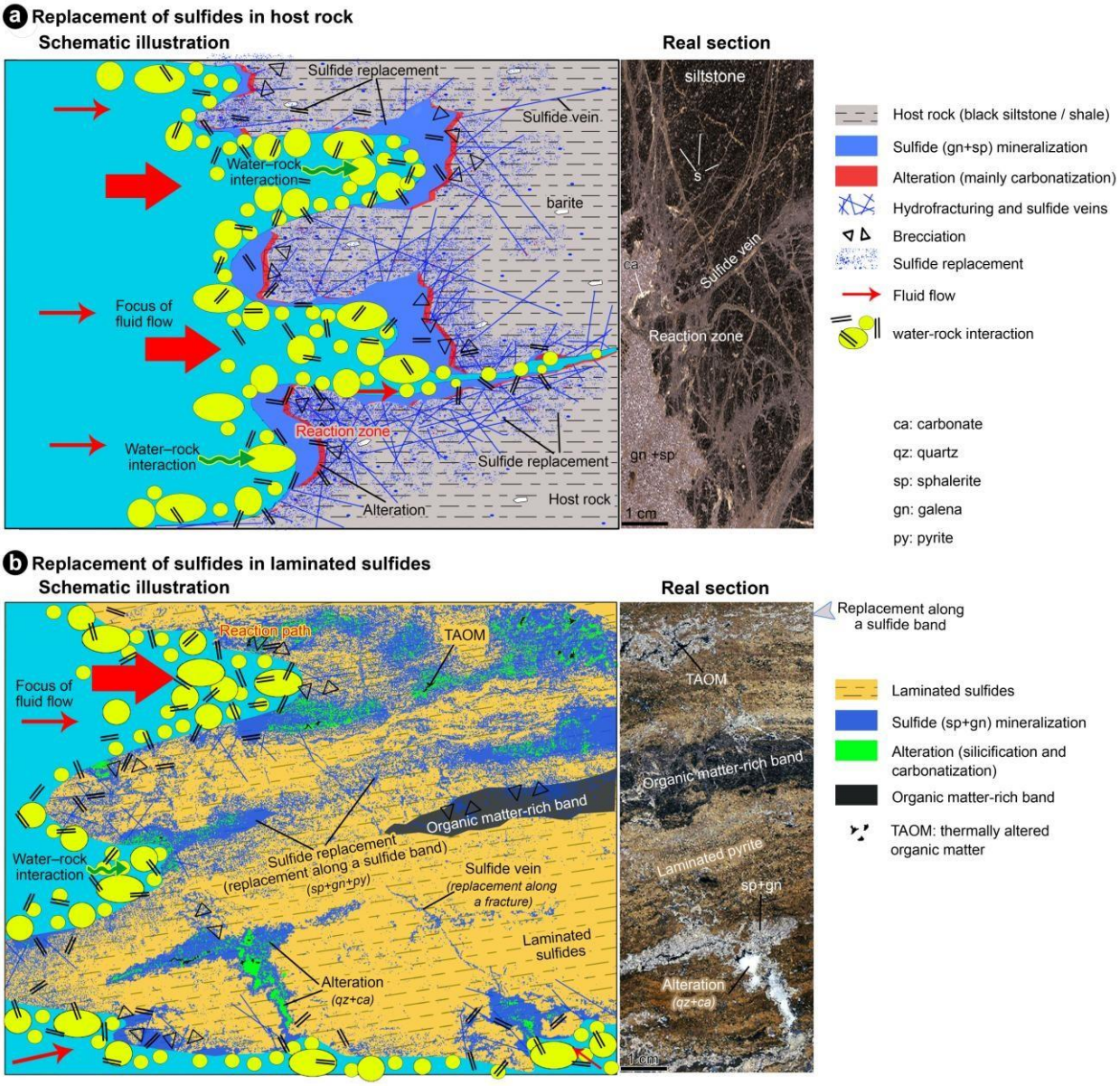

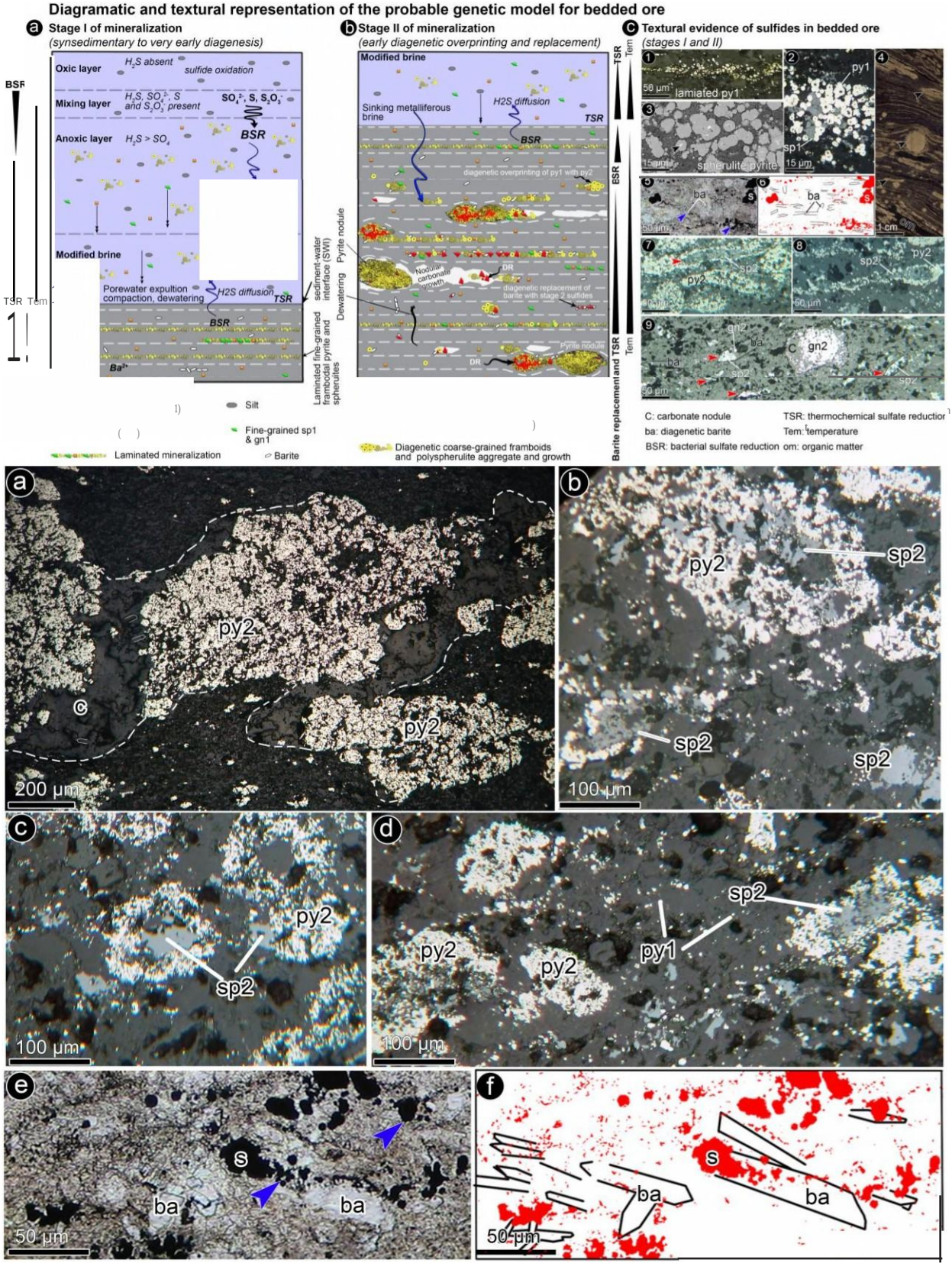
Diagramatic and textural representation of the probable genetic model for bedded ore
a Stage I of mineralization
(synsedimentary to very early diagenesis)
b Stage II of mineralization
(early diagenetic overprinting and replacement)
c Textural evidence of sulfides in bedded ore
(stages I and II)
Oxic layer
Mixing layer
Anoxic layer
Modified brine
Porewater expultion compaction, dewatering
Sinking metalliferous brine
Pyrite nodule
Dewatering
Laminated fine-grained framboidal pyrite and spherulites
Diagenetic overprinting of py1 with py2
Nodular carbonate growth
diagenetic replacement of barite with stage 2 sulfides
Barite replacement and TSR
lamiated py1
spherulite pyrite
C: carbonate nodule
ba: diagenetic barite
BSR: bacterial sulfate reduction
TSR: thermochemical sulfate reduction
Tem: temperature
om: organic matter
Silt
Fine-grained sp1 & gn1
Laminated mineralization
Barite
Diagenetic coarse-grained framboids and polyspherulite aggregate and growth
a
py2
c
200 μm
b
sp2
100 μm
c
100 μm
d
py1
e
s
50 μm
f

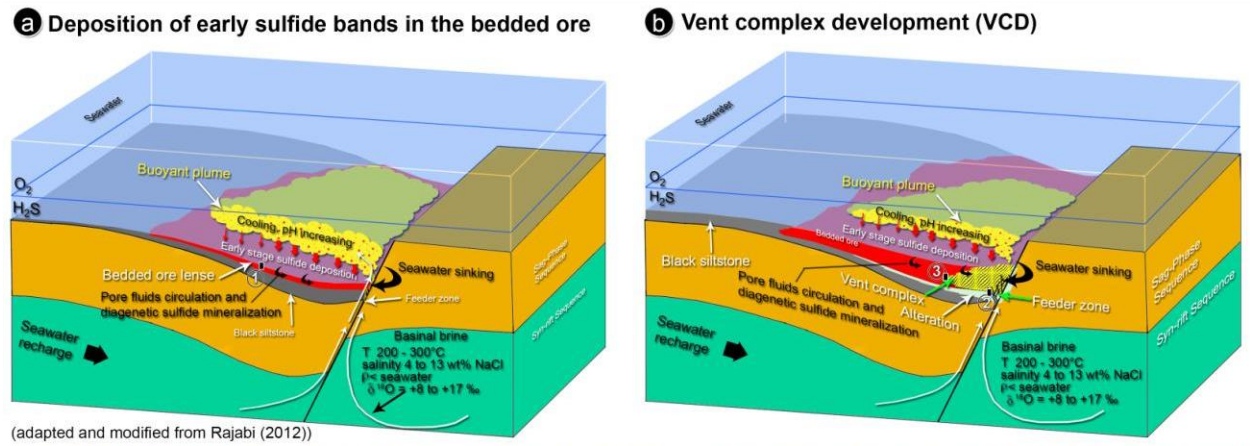
a Deposition of early sulfide bands in the bedded ore
b Vent complex development (VCD)
Seawater
Buoyant plume
Cooling, pH increasing
Early stage sulfide deposition
Bedded ore lense
Pore fluids circulation and diagenetic sulfide mineralization
Seawater sinking
Feeder zone
Black siltstone
Seawater recharge
Basinal brine
T 200 - 300°C
salinity 4 to 13 wt% NaCl
ρ< seawater
δ 18O = +8 to +17 ‰
Vent complex
Alteration
Syn-rift Sequence
(adapted and modified from Rajabi (2012))

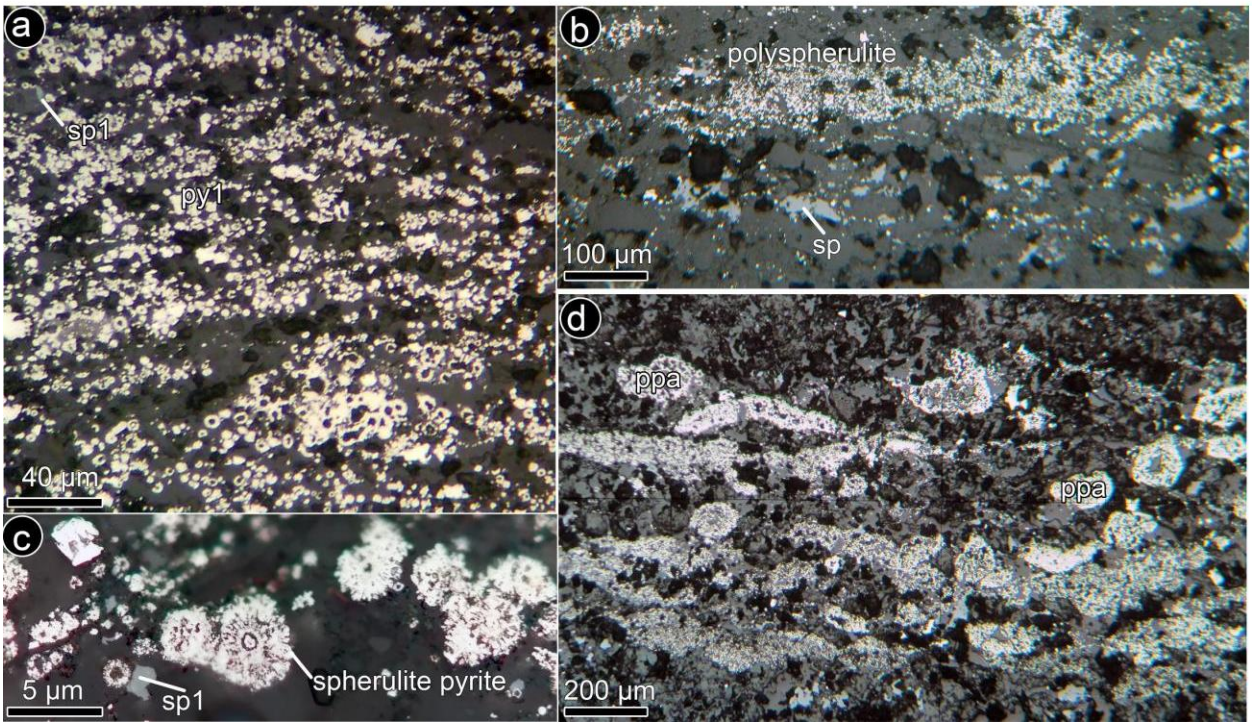
a
sp1
py1
40 µm
b
polyspherulite
sp
100 µm
c
5 µm
sp1
spherulite pyrite
d
ppa
ppa
200 µm

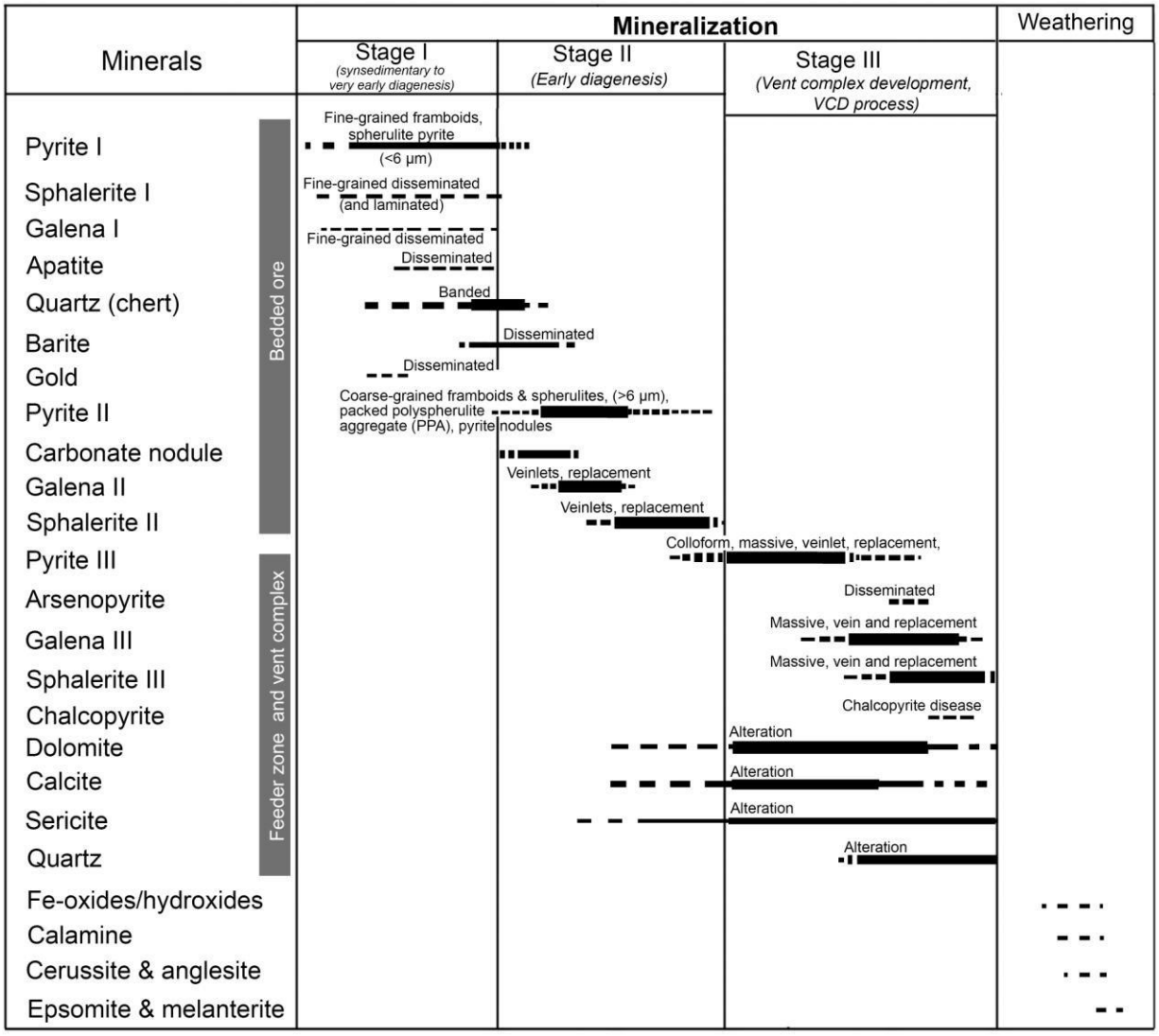
Minerals
Mineralization
Weathering
Stage I
(synsedimentary to very early diagenesis)
Stage II
(Early diagenesis)
Stage III
(Vent complex development, VCD process)
Bedded ore
Feeder zone and vent complex
Pyrite I
Sphalerite I
Galena I
Apatite
Quartz (chert)
Barite
Gold
Pyrite II
Carbonate nodule
Galena II
Sphalerite II
Pyrite III
Arsenopyrite
Galena III
Sphalerite III
Chalcopyrite
Dolomite
Calcite
Sericite
Quartz
Fe-oxides/hydroxides
Calamine
Cerussite & anglesite
Epsomite & melanterite
Fine-grained framboids, spherulite pyrite (<6 μm)
Fine-grained disseminated (and laminated)
Fine-grained disseminated
Disseminated
Banded
Disseminated
Disseminated
Coarse-grained framboids & spherulites, (>6 μm), packed polyspherulite aggregate (PPA), pyrite nodules
Veinlets, replacement
Veinlets, replacement
Colloform, massive, veinlet, replacement,
Disseminated
Massive, vein and replacement
Massive, vein and replacement
Chalcopyrite disease
Alteration
Alteration
Alteration
Alteration

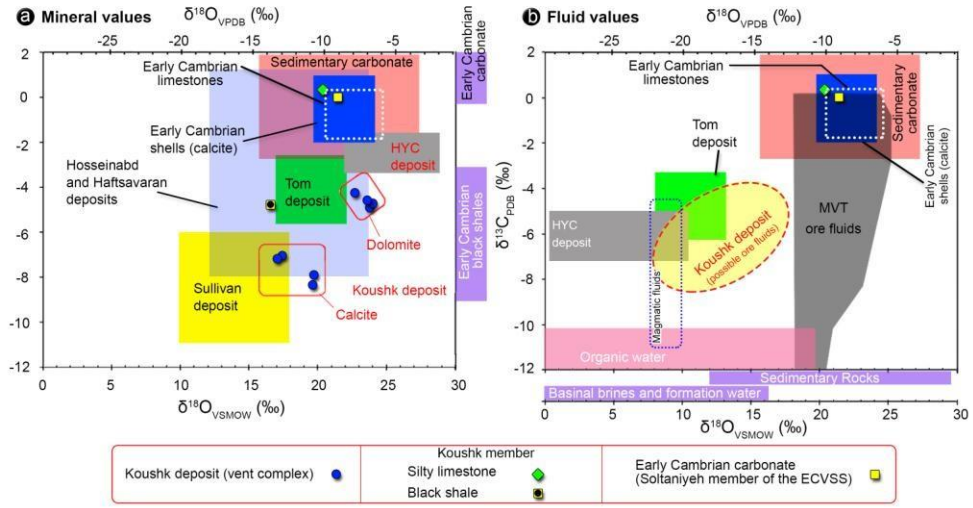
a Mineral values
δ18OVPDB (‰)
δ18OVSMOW (‰)
Early Cambrian limestones
Sedimentary carbonate
Early Cambrian shells (calcite)
HYC deposit
Hosseinabd and Haftsavaran deposits
Tom deposit
Dolomite
Sullivan deposit
Koushk deposit
Calcite
Early Cambrian carbonate
Early Cambrian black shales
b Fluid values
δ13CPDB (‰)
Tom deposit
MVT ore fluids
Koushk deposit (possible ore fluids)
Magmatic fluids
Organic water
Sedimentary Rocks
Basinal brines and formation water
Koushk deposit (vent complex)
Koushk member
Silty limestone
Black shale
Early Cambrian carbonate (Soltaniyeh member of the ECVSS)

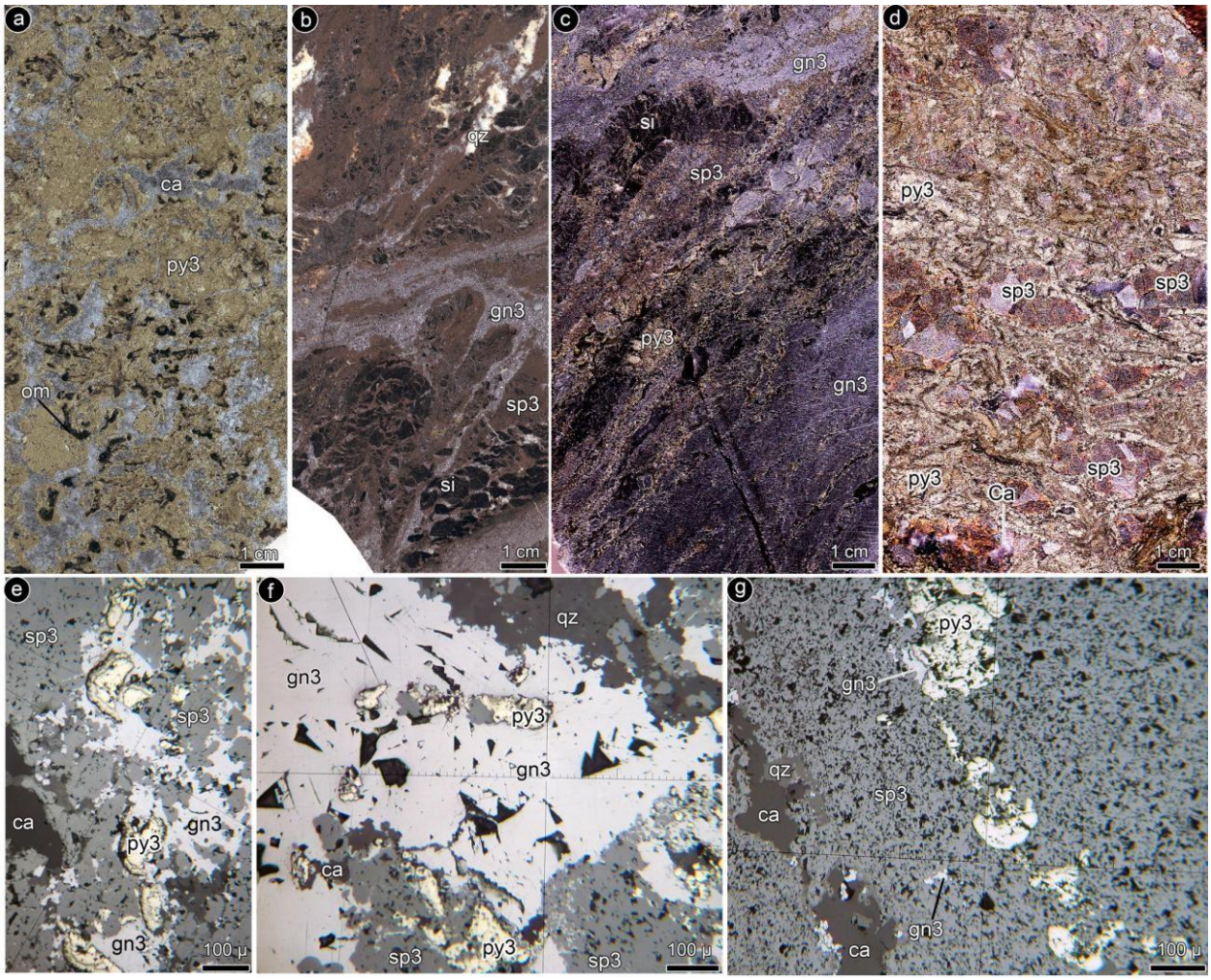
a
ca
py3
om
1 cm
b
qz
gn3
sp3
si
1 cm
c
gn3
si
sp3
py3
gn3
1 cm
d
py3
sp3
sp3
py3
Ca
sp3
1 cm
e
sp3
sp3
ca
py3
gn3
gn3
100 µ
f
qz
gn3
py3
gn3
ca
sp3
py3
sp3
100 µ
g
py3
gn3
qz
sp3
ca
gn3
ca
100 µ

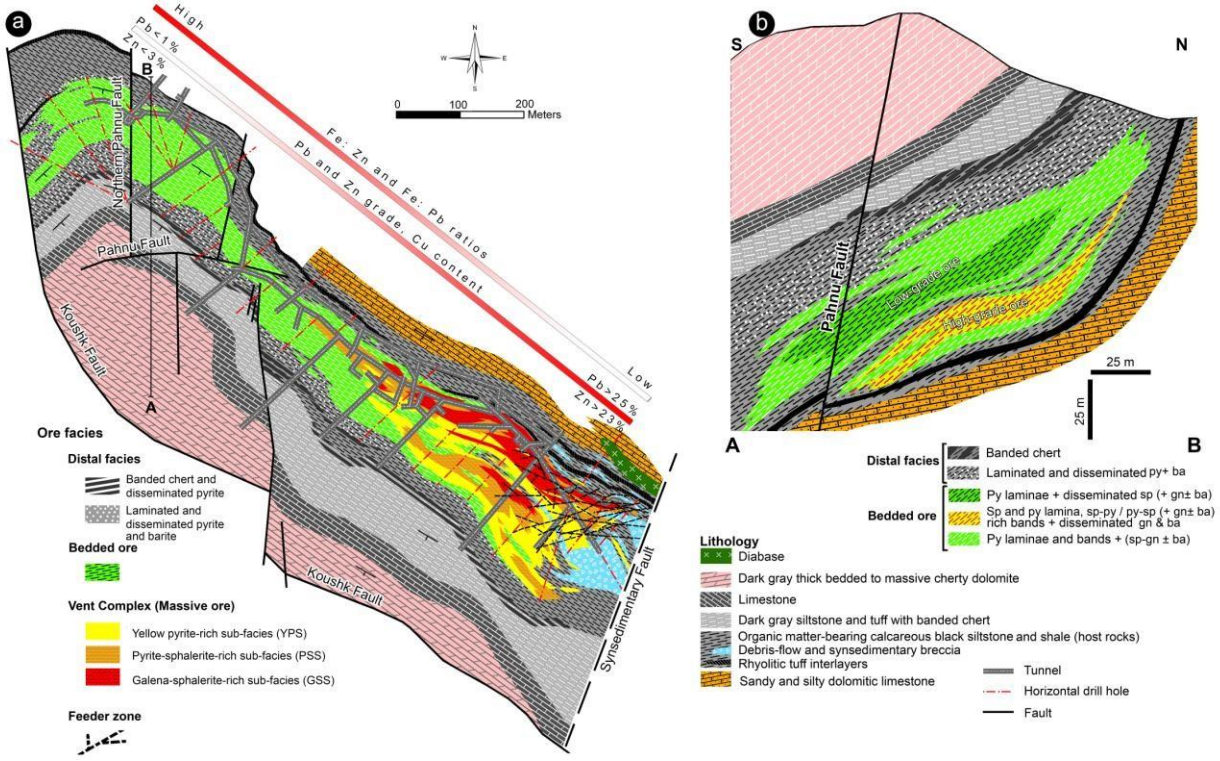
a
High
Pb<1%
Zn<3%
B
Northern Pannu Fault
Pahnu Fault
Koushk Fault
A
Fe: Zn and Fe: Pb ratios
Pb and Zn grade; Cu content
Low
Pb>25%
Zn>23%
Koushk Fault
Synsedimentary Fault
0 100 200 Meters
Ore facies
Distal facies
Banded chert and disseminated pyrite
Laminated and disseminated pyrite and barite
Bedded ore
Vent Complex (Massive ore)
Yellow pyrite-rich sub-facies (YPS)
Pyrite-sphalerite-rich sub-facies (PSS)
Galena-sphalerite-rich sub-facies (GSS)
Feeder zone
b
S
N
Pahnu Fault
Low-grade ore
High-grade ore
25 m
25 m
A
B
Distal facies
Banded chert
Laminated and disseminated py+ ba
Bedded ore
Py laminae + disseminated sp (+ gn± ba)
Sp and py lamina, sp-py / py-sp (+ gn± ba) rich bands + disseminated gn & ba
Py laminae and bands + (sp-gn ± ba)
Lithology
Diabase
Dark gray thick bedded to massive cherty dolomite
Limestone
Dark gray siltstone and tuff with banded chert
Organic matter-bearing calcareous black siltstone and shale (host rocks)
Debris-flow and synsedimentary breccia
Rhyolitic tuff interlayers
Sandy and silty dolomitic limestone
Tunnel
Horizontal drill hole
Fault

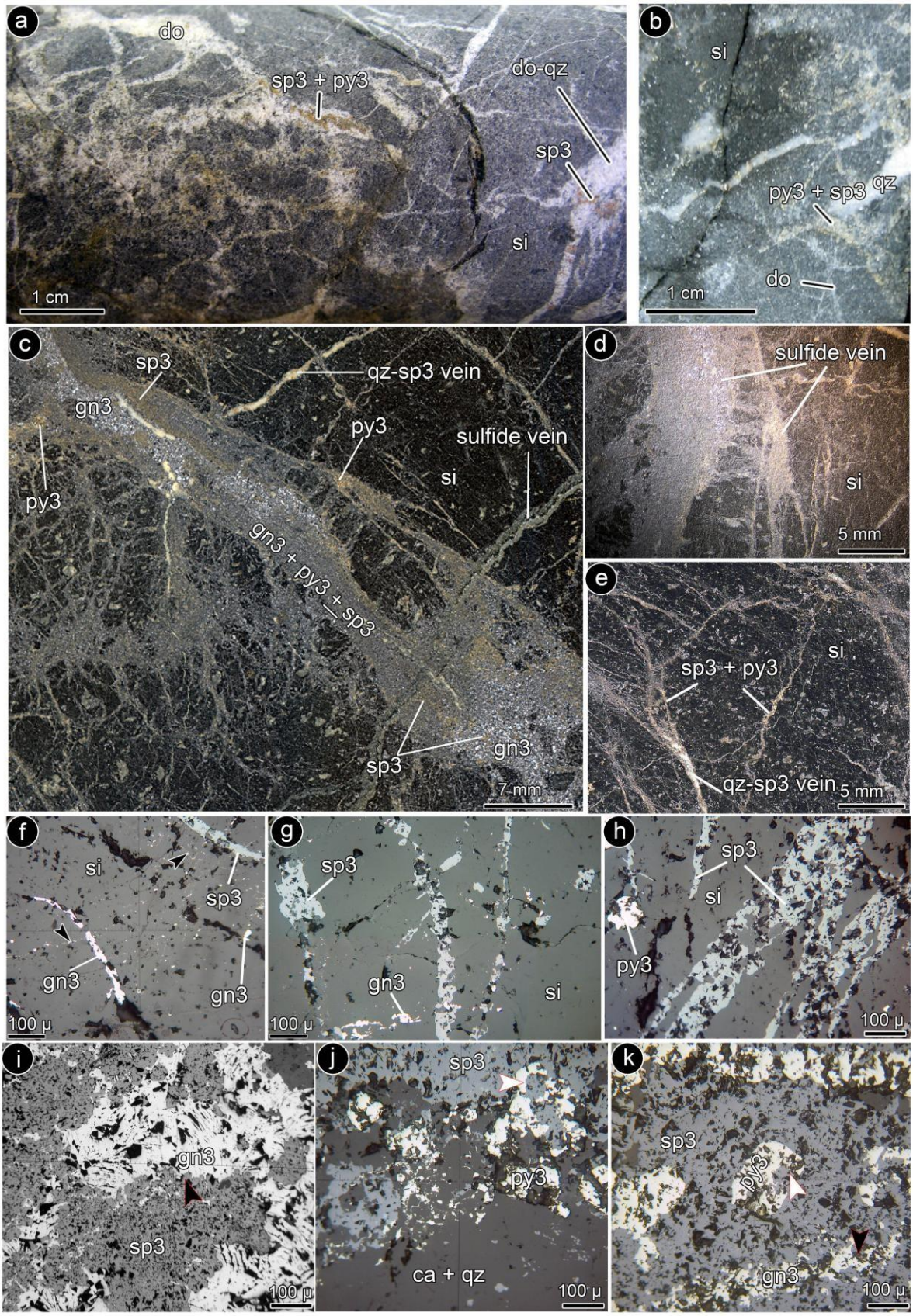
a
do
sp3 + py3
do-qz
sp3
si
1 cm
b
si
py3 + sp3 qz
do
1 cm
c
sp3
qz-sp3 vein
gn3
py3
py3
sulfide vein
si
gn3 + py3 + sp3
sp3
gn3
7 mm
d
sulfide vein
si
5 mm
e
si
sp3 + py3
qz-sp3 vein
5 mm
f
si
sp3
gn3
gn3
100 µ
g
sp3
gn3
si
100 µ
h
sp3
si
py3
100 µ
i
gn3
sp3
100 µ
j
sp3
py3
ca + qz
100 µ
k
sp3
py3
gn3
100 µ

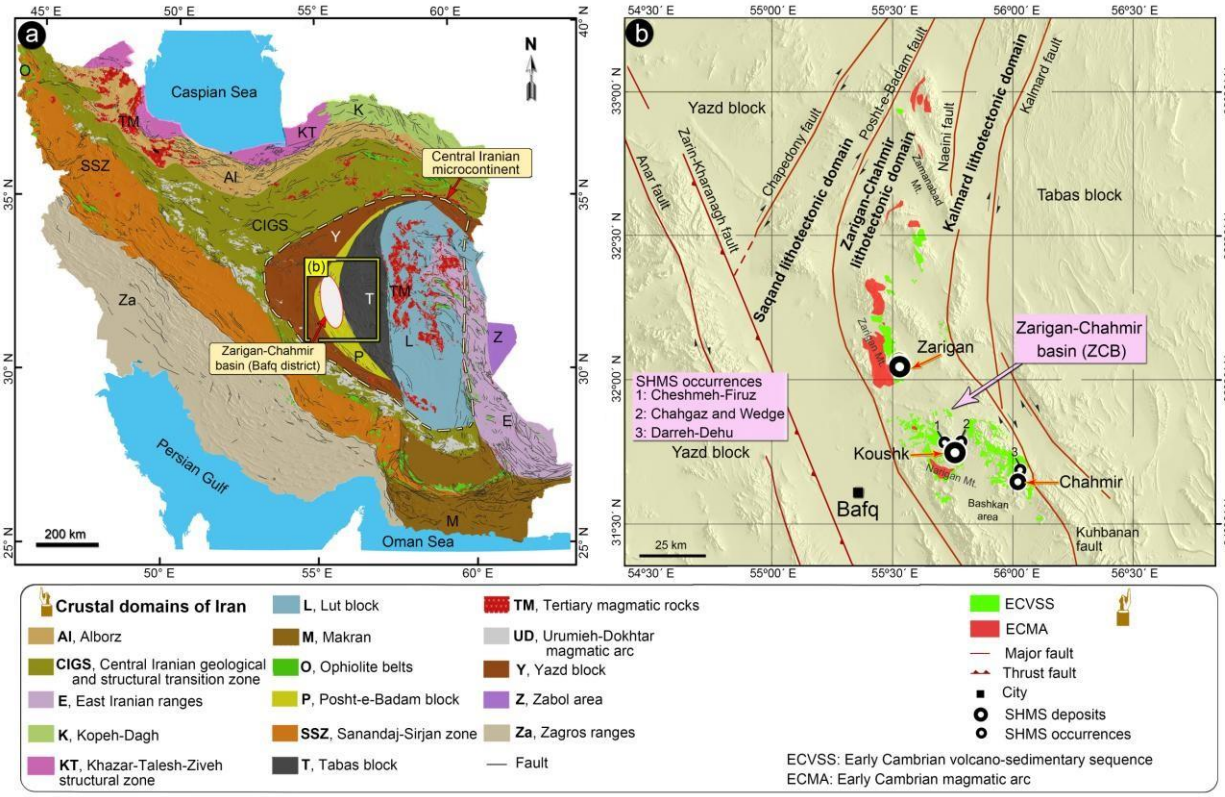
a
b
Caspian Sea
Persian Gulf
Oman Sea
Central Iranian microcontinent
Zarigan-Chahmir basin (Bafq district)
200 km
Yazd block
Tabas block
Saqand lithotectonic domain
Zarigan-Chahmir lithotectonic domain
Kalmard lithotectonic domain
Anar fault
Zarin-Kharanagh fault
Chapedony fault
Posht-e-Badam fault
Naeini fault
Kalmard fault
Zarigan
Zarigan-Chahmir basin (ZCB)
SHMS occurrences
1: Cheshmeh-Firuz
2: Chahgaz and Wedge
3: Darreh-Dehu
Koushk
Chahmir
Bafq
Bashkan area
Kuhbanan fault
25 km
Crustal domains of Iran
AI, Alborz
CIGS, Central Iranian geological and structural transition zone
E, East Iranian ranges
K, Kopeh-Dagh
KT, Khazar-Talesh-Ziveh structural zone
L, Lut block
M, Makran
O, Ophiolite belts
P, Posht-e-Badam block
SSZ, Sanandaj-Sirjan zone
T, Tabas block
TM, Tertiary magmatic rocks
UD, Urumieh-Dokhtar magmatic arc
Y, Yazd block
Z, Zabol area
Za, Zagros ranges
Fault
ECVSS
ECMA
Major fault
Thrust fault
City
SHMS deposits
SHMS occurrences
ECVSS: Early Cambrian volcano-sedimentary sequence
ECMA: Early Cambrian magmatic arc

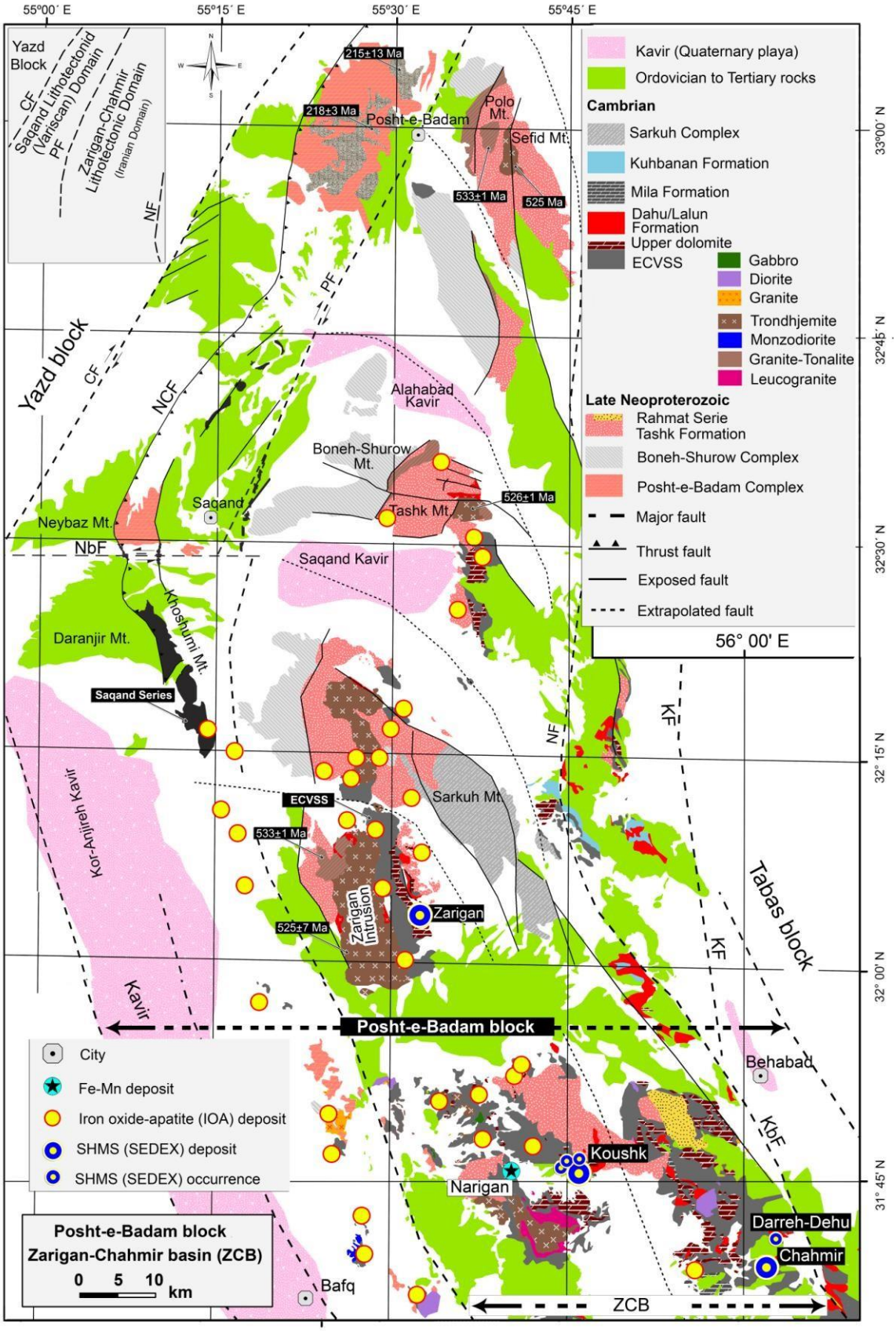
55°00´ E
55°15´ E
55°30´ E
55°45´ E
33°00´ N
32°45´ N
32°30´ N
32° 15´ N
32° 00´ N
31° 45´ N
56° 00' E
Yazd Block
CF
Saqand Lithotectonid (Variscan) Domain
PF
Zarigan-Chahmir Lithotectonic Domain
(Iranian Domain)
NF
Yazd block
CF
NCF
PF
NbF
KF
Tabas block
KbF
Kavir
Kor-Arjiyeh Kavir
Alahabad Kavir
Saqand Kavir
Khoshumi Mt.
Daranjir Mt.
Neybaz Mt.
Saqand
Boneh-Shurow Mt.
Tashk Mt.
Polo Mt.
Sefid Mt.
Posht-e-Badam
Sarkuh Mt.
Zarigan Intrusion
Zarigan
Koushk
Narigan
Darreh-Dehu
Chahmir
Behabad
Bafq
Saqand Series
ECVSS
215±13 Ma
218±3 Ma
533±1 Ma
525 Ma
526±1 Ma
525±7 Ma
Posht-e-Badam block
ZCB
Kavir (Quaternary playa)
Ordovician to Tertiary rocks
Cambrian
Sarkuh Complex
Kuhbanan Formation
Mila Formation
Dahu/Lalun Formation
Upper dolomite
ECVSS
Gabbro
Diorite
Granite
Trondhjemite
Monzodiorite
Granite-Tonalite
Leucogranite
Late Neoproterozoic
Rahmat Serie
Tashk Formation
Boneh-Shurow Complex
Posht-e-Badam Complex
Major fault
Thrust fault
Exposed fault
Extrapolated fault
City
Fe-Mn deposit
Iron oxide-apatite (IOA) deposit
SHMS (SEDEX) deposit
SHMS (SEDEX) occurrence
Posht-e-Badam block
Zarigan-Chahmir basin (ZCB)
0 5 10 km

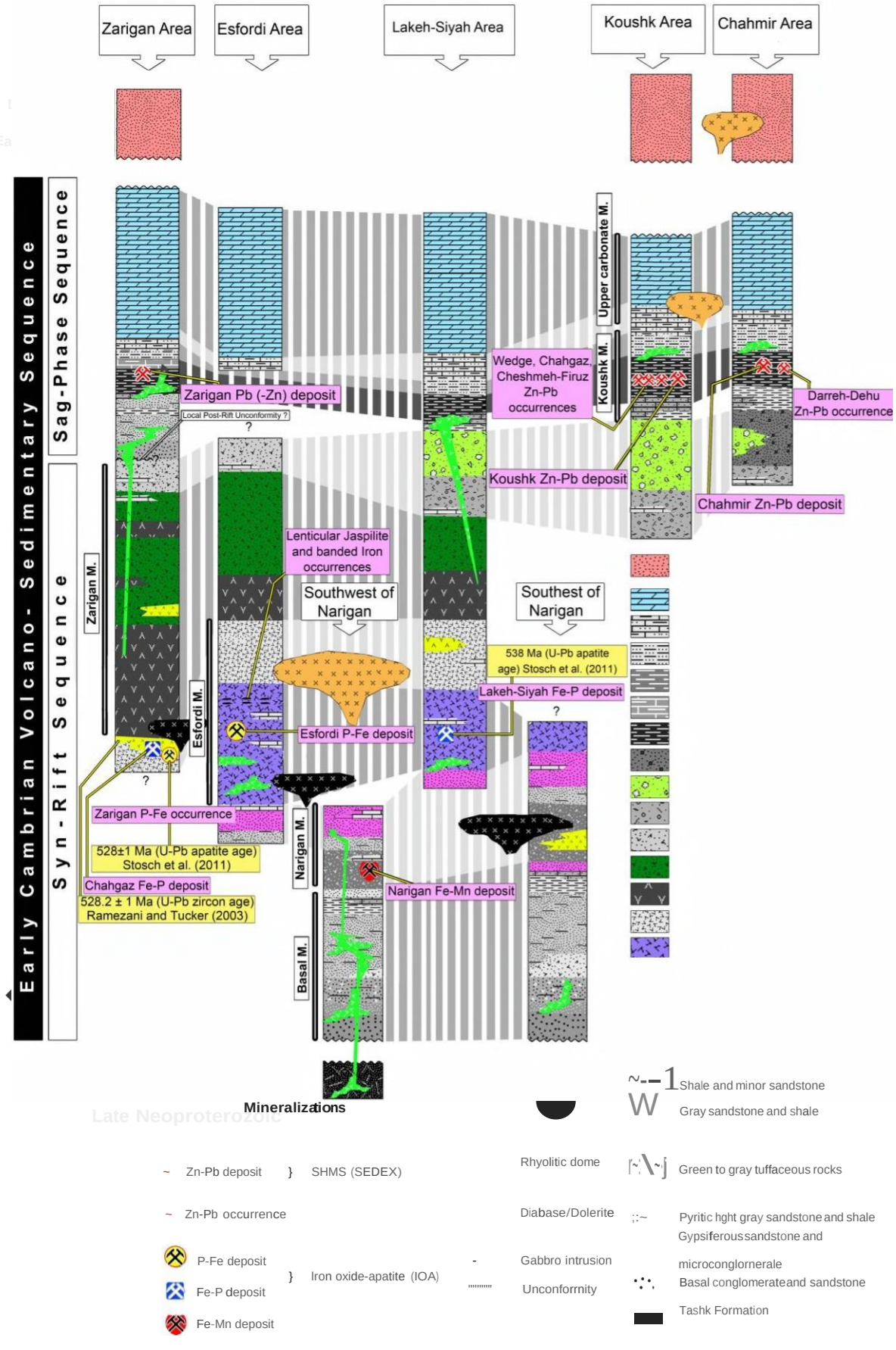
Zarigan Area
Esfordi Area
Lakeh-Siyah Area
Koushk Area
Chahmir Area
Early Cambrian Volcano- Sedimentary Sequence
Syn-Rift Sequence
Sag-Phase Sequence
Upper carbonate M.
Koushk M.
Zarigan M.
Esfordi M.
Narigan M.
Basal M.
Zarigan Pb (-Zn) deposit
Local Post-Rift Unconformity ?
Wedge, Chahgaz, Cheshmeh-Firuz Zn-Pb occurrences
Darreh-Dehu Zn-Pb occurrence
Koushk Zn-Pb deposit
Chahmir Zn-Pb deposit
Lenticular Jaspilite and banded Iron occurrences
Southwest of Narigan
Southest of Narigan
538 Ma (U-Pb apatite age) Stosch et al. (2011)
Lakeh-Siyah Fe-P deposit
Esfordi P-Fe deposit
Zarigan P-Fe occurrence
528±1 Ma (U-Pb apatite age) Stosch et al. (2011)
Chahgaz Fe-P deposit
528.2 ± 1 Ma (U-Pb zircon age) Ramezani and Tucker (2003)
Narigan Fe-Mn deposit
Mineralizations
Late Neoproterozoic
Shale and minor sandstone
Gray sandstone and shale
Zn-Pb deposit
SHMS (SEDEX)
Zn-Pb occurrence
P-Fe deposit
Fe-P deposit
Fe-Mn deposit
Iron oxide-apatite (IOA)
Rhyolitic dome
Diabase/Dolerite
Gabbro intrusion
Unconformity
Green to gray tuffaceous rocks
Pyritic hght gray sandstone and shale
Gypsiferous sandstone and microconglornerale
Basal conglomerate and sandstone
Tashk Formation

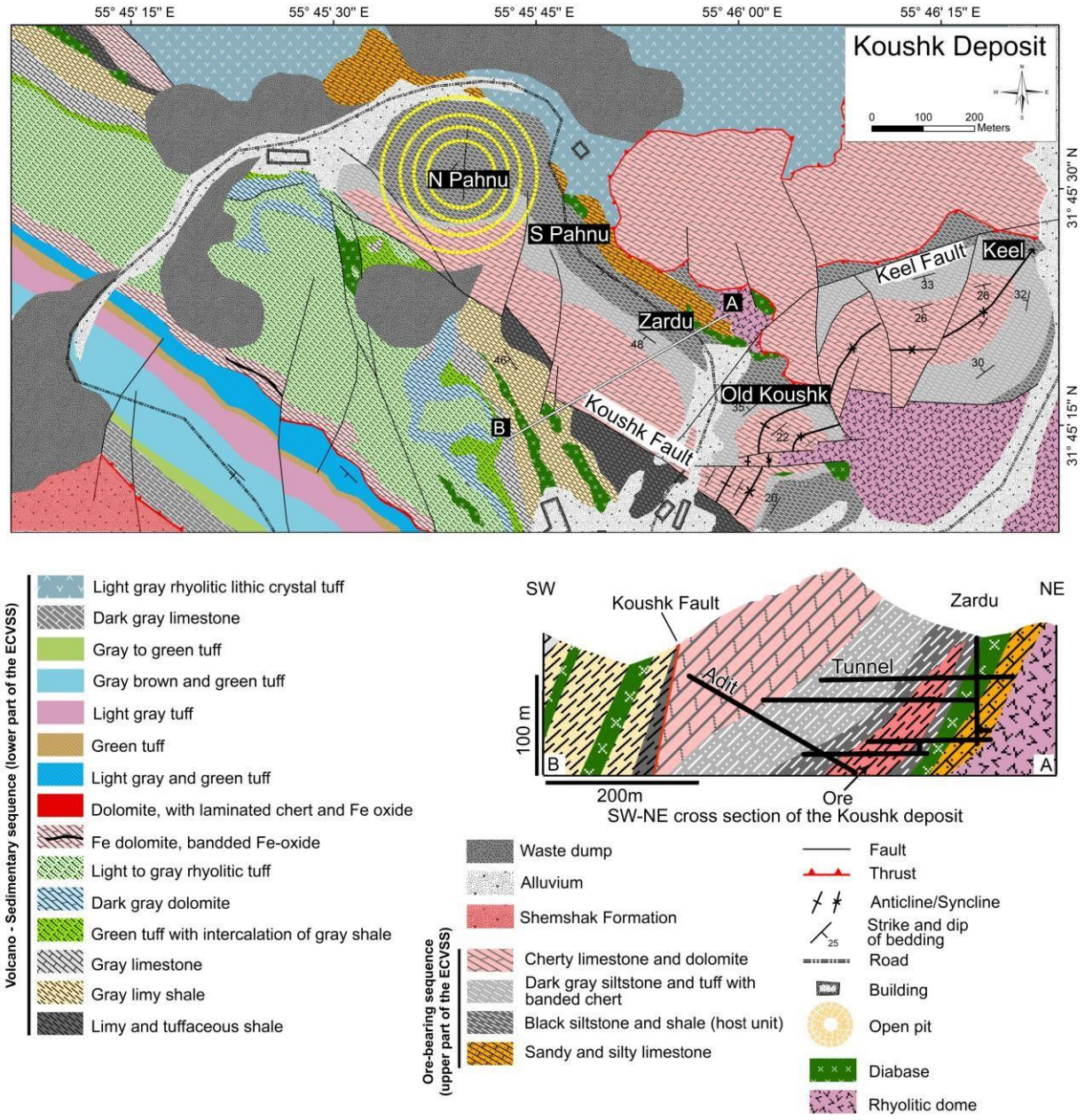
55° 45' 15" E
55° 45' 30" E
55° 45' 45" E
55° 46' 00" E
55° 46' 15" E
31° 45' 30" N
31° 45' 15" N
Koushk Deposit
0 100 200 Meters
N Pahnu
S Pahnu
Keel Fault
Keel
Zardu
A
B
Koushk Fault
Old Koushk
Volcano - Sedimentary sequence (lower part of the ECVSS)
Light gray rhyolitic lithic crystal tuff
Dark gray limestone
Gray to green tuff
Gray brown and green tuff
Light gray tuff
Green tuff
Light gray and green tuff
Dolomite, with laminated chert and Fe oxide
Fe dolomite, bandded Fe-oxide
Light to gray rhyolitic tuff
Dark gray dolomite
Green tuff with intercalation of gray shale
Gray limestone
Gray limy shale
Limy and tuffaceous shale
SW
NE
Koushk Fault
Zardu
Adit
Tunnel
100 m
200m
Ore
SW-NE cross section of the Koushk deposit
Waste dump
Alluvium
Shemshak Formation
Ore-bearing sequence (upper part of the ECVSS)
Cherty limestone and dolomite
Dark gray siltstone and tuff with banded chert
Black siltstone and shale (host unit)
Sandy and silty limestone
Fault
Thrust
Anticline/Syncline
Strike and dip of bedding
Road
Building
Open pit
Diabase
Rhyolitic dome

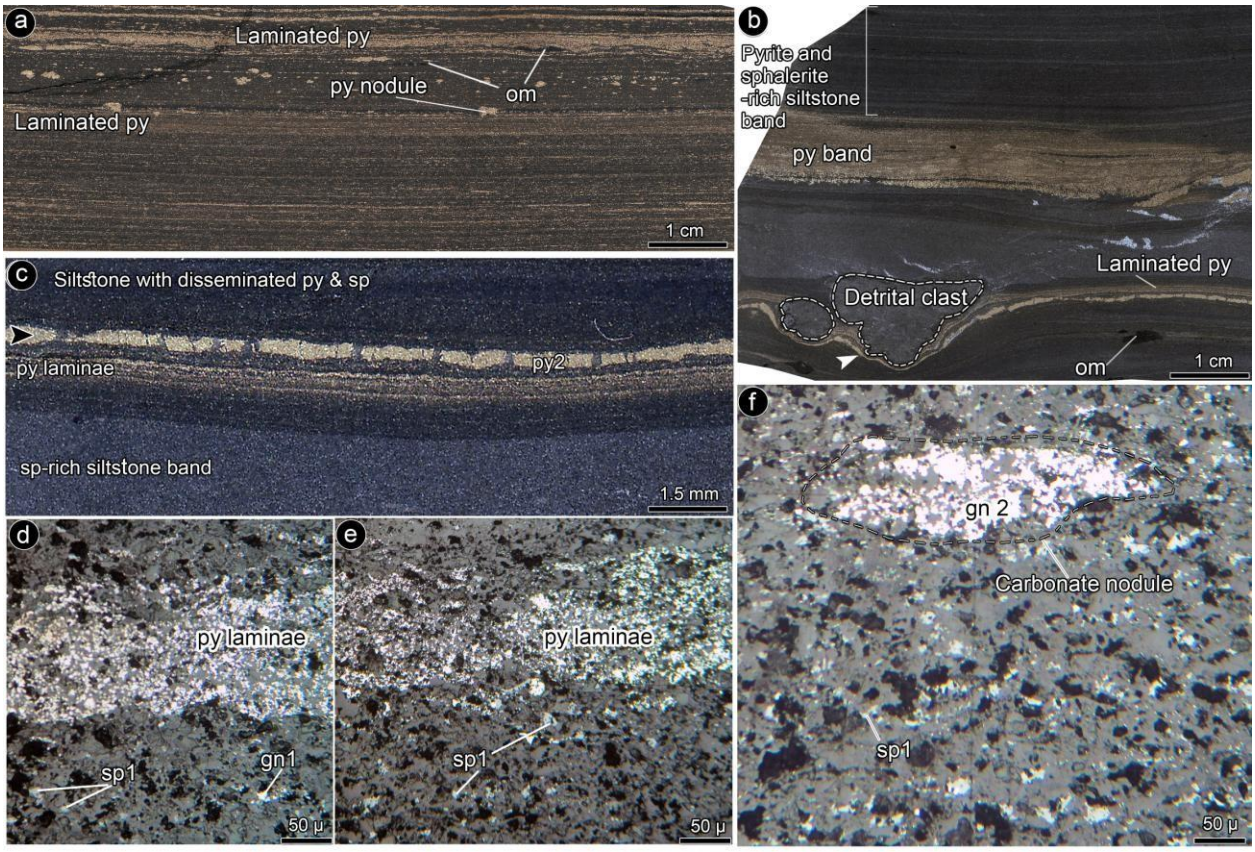
a
Laminated py
py nodule
om
Laminated py
1 cm
b
Pyrite and sphalerite -rich siltstone band
py band
Laminated py
Detrital clast
om
1 cm
c
Siltstone with disseminated py & sp
py laminae
py2
sp-rich siltstone band
1.5 mm
d
py laminae
sp1
gn1
50 µ
e
py laminae
sp1
50 µ
f
gn 2
Carbonate nodule
sp1
50 µ

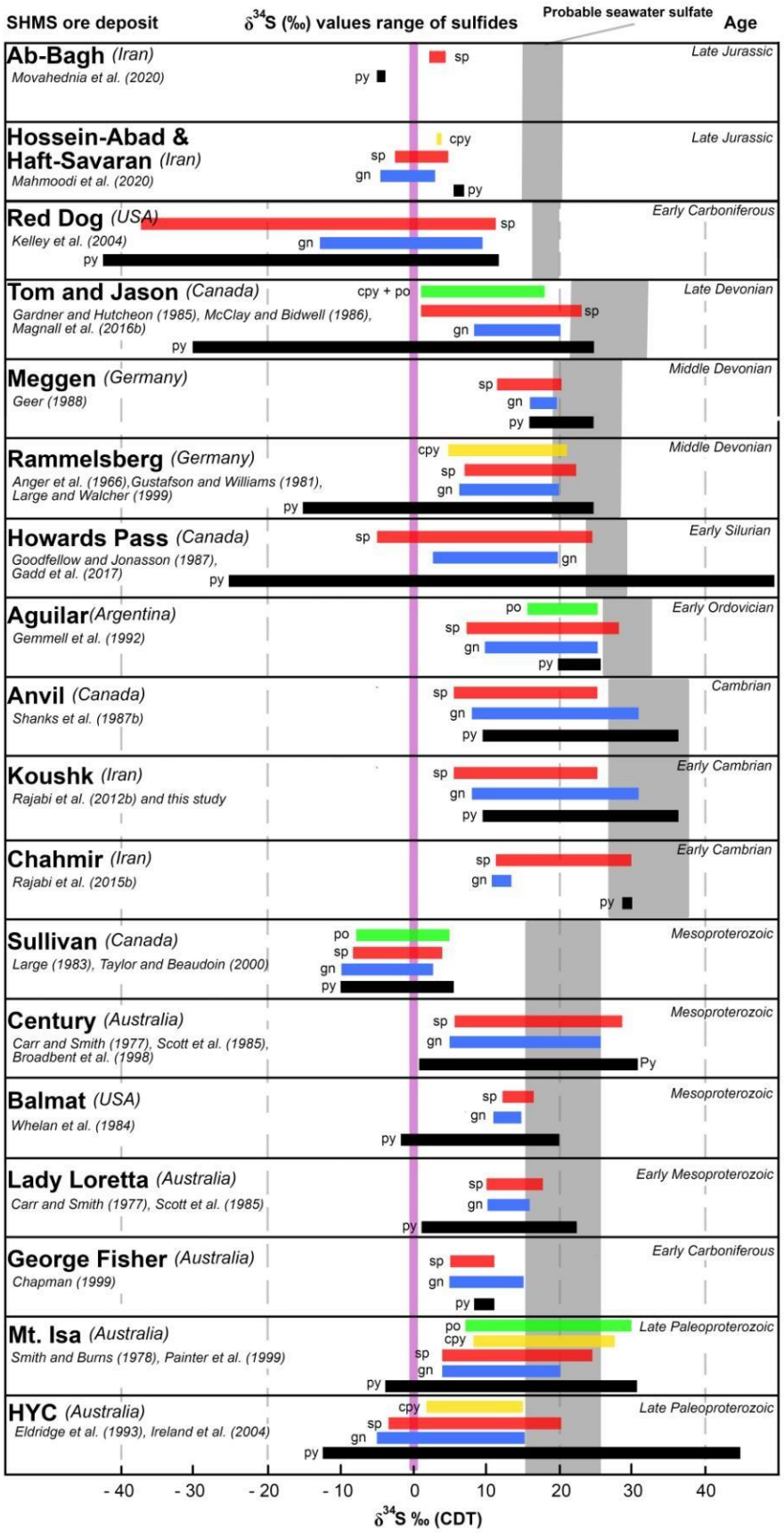
SHMS ore deposit
δ34S (‰) values range of sulfides
Probable seawater sulfate
Age
Ab-Bagh (Iran)
Movahednia et al. (2020)
Late Jurassic
Hossein-Abad & Haft-Savaran (Iran)
Mahmoodi et al. (2020)
Late Jurassic
Red Dog (USA)
Kelley et al. (2004)
Early Carboniferous
Tom and Jason (Canada)
Gardner and Hutcheon (1985), McClay and Bidwell (1986), Magnall et al. (2016b)
Late Devonian
Meggen (Germany)
Geer (1988)
Middle Devonian
Rammelsberg (Germany)
Anger et al. (1966),Gustafson and Williams (1981), Large and Walcher (1999)
Middle Devonian
Howards Pass (Canada)
Goodfellow and Jonasson (1987), Gadd et al. (2017)
Early Silurian
Aguilar(Argentina)
Gemmell et al. (1992)
Early Ordovician
Anvil (Canada)
Shanks et al. (1987b)
Cambrian
Koushk (Iran)
Rajabi et al. (2012b) and this study
Early Cambrian
Chahmir (Iran)
Rajabi et al. (2015b)
Early Cambrian
Sullivan (Canada)
Large (1983), Taylor and Beaudoin (2000)
Mesoproterozoic
Century (Australia)
Carr and Smith (1977), Scott et al. (1985), Broadbent et al. (1998)
Mesoproterozoic
Balmat (USA)
Whelan et al. (1984)
Mesoproterozoic
Lady Loretta (Australia)
Carr and Smith (1977), Scott et al. (1985)
Early Mesoproterozoic
George Fisher (Australia)
Chapman (1999)
Early Carboniferous
Mt. Isa (Australia)
Smith and Burns (1978), Painter et al. (1999)
Late Paleoproterozoic
HYC (Australia)
Eldridge et al. (1993), Ireland et al. (2004)
Late Paleoproterozoic
sp
py
cpy
gn
po
cpy + po
Py
- 40
- 30
- 20
- 10
0
10
20
30
40
δ34S ‰ (CDT)

Textural relationships and S isotope data reveal that the contribution of TSR and direct barite replacement are so significant in Zn-Pb mineralization of the vent-proximal SHMS deposits.

Vent-proximal SHMS deposits formed predominantly during the diagenesis in the uppermost sediment pile and replacement of host rocks during VCD processes.

Conflicts of Interest Statement

Manuscript title: The world-class Koushk Zn-Pb deposit, Central Iran: a genetic model for vent-proximal shale-hosted massive sulfide (SHMS) deposits – based on paragenesis and stable isotope geochemistry

The authors whose names are listed immediately below certify that they have NO affiliations with or involvement in any organization or entity with any financial interest (such as honoraria; educational grants; participation in speakers' bureaus; membership, employment, consultancies, stock ownership, or other equity interest; and expert testimony or patent-licensing arrangements), or non-financial interest (such as personal or professional relationships, affiliations, knowledge or beliefs) in the subject matter or materials discussed in this manuscript.

Abdorrahman Rajabi[a]*, Pura Alfonso[b], Carles Canet[c], Ebrahim Rastad[d], Shojaedin Niroomand[a], Soroush Modabberi[a], Pouria Mahmoodi[d]

a- School of Geology, College of Science, University of Tehran, Tehran, Iran

b- Dept. d'Enginyeria Minera, Industrial i TIC, Universitat Politècnica de Catalunya, Av. de les Bases de Manresa 61-73 o8242 Manresa, Spain

c- Centro de Ciencias de la Atmósfera, Universidad Nacional Autónoma de México, Del. Coyoacán, 04150 Ciudad de México, Mexico

d- Department of Geology, Faculty of Basic Sciences, Tarbiat Modares University, Tehran 14115-175, Iran

Rajabi

University of Tehran

Rahman.rajabi@ut.ac.ir

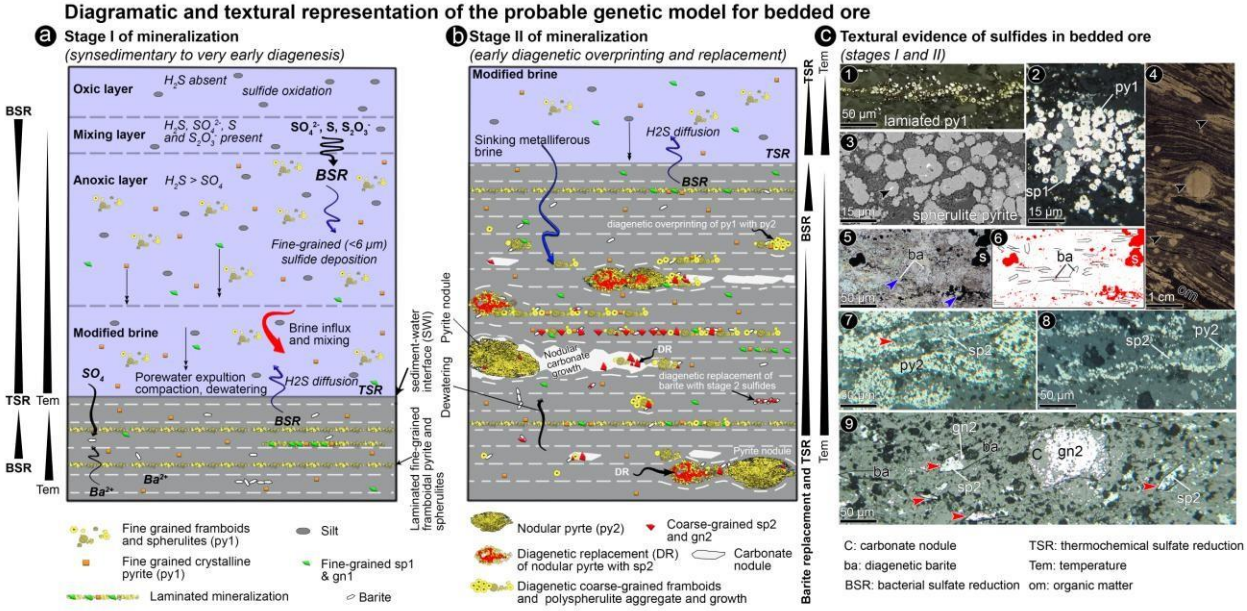
Diagramatic and textural representation of the probable genetic model for bedded ore
a Stage I of mineralization
(synsedimentary to very early diagenesis)
b Stage II of mineralization
(early diagenetic overprinting and replacement)
c Textural evidence of sulfides in bedded ore
(stages I and II)
Oxic layer
Mixing layer
Anoxic layer
Modified brine
Brine influx and mixing
Porewater expultion compaction, dewatering
Fine-grained (<6 µm) sulfide deposition
sulfide oxidation
BSR
TSR
Tem
Sinking metalliferous brine
H2S diffusion
diagenetic overprinting of py1 with py2
Nodular carbonate growth
diagenetic replacement of barite with stage 2 sulfides
Pyrite nodule
DR
sediment-water interface (SWI)
Dewatering
Laminated fine-grained framboidal pyrite and spherulites
Barite replacement and TSR
lamiated py1
spherulite pyrite
py1
sp1
ba
py2
sp2
gn2
C
1 cm
Fine grained framboids and spherulites (py1)
Fine grained crystalline pyrite (py1)
Laminated mineralization
Silt
Fine-grained sp1 & gn1
Barite
Nodular pyrte (py2)
Coarse-grained sp2 and gn2
Diagenetic replacement (DR) of nodular pyrte with sp2
Carbonate nodule
Diagenetic coarse-grained framboids and polyspherulite aggregate and growth
C: carbonate nodule
ba: diagenetic barite
BSR: bacterial sulfate reduction
TSR: thermochemical sulfate reduction
Tem: temperature
om: organic matter

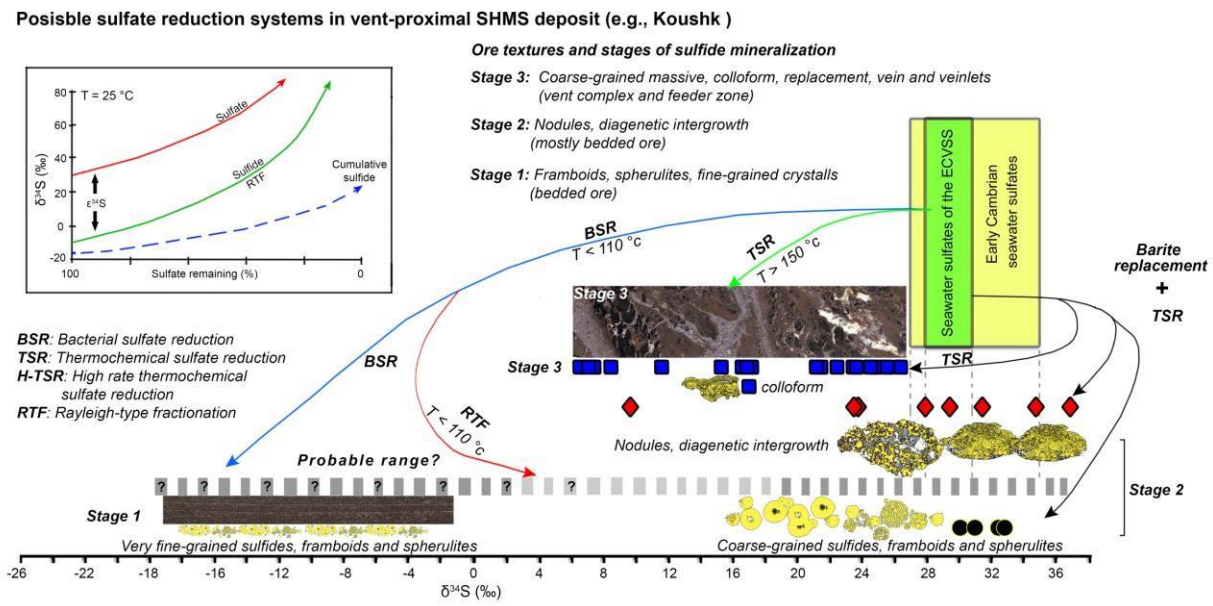
Posisble sulfate reduction systems in vent-proximal SHMS deposit (e.g., Koushk)
T = 25 °C
Sulfate
Sulfide
RTF
Cumulative sulfide
ε34S
δ34S (‰)
Sulfate remaining (%)
BSR: Bacterial sulfate reduction
TSR: Thermochemical sulfate reduction
H-TSR: High rate thermochemical sulfate reduction
RTF: Rayleigh-type fractionation
Ore textures and stages of sulfide mineralization
Stage 3: Coarse-grained massive, colloform, replacement, vein and veinlets (vent complex and feeder zone)
Stage 2: Nodules, diagenetic intergrowth (mostly bedded ore)
Stage 1: Framboids, spherulites, fine-grained crystalls (bedded ore)
Seawater sulfates of the ECVSS
Early Cambrian seawater sulfates
BSR
T < 110 °c
TSR
T > 150 °c
Barite replacement + TSR
Stage 3
colloform
Nodules, diagenetic intergrowth
Stage 2
RTF
T < 110 °c
Probable range?
Stage 1
Very fine-grained sulfides, framboids and spherulites
Coarse-grained sulfides, framboids and spherulites
δ34S (‰)